Geothermal Energy

RESEARCH Open Access

Seismicity induced during the development of the Rittershoffen geothermal field, France

Vincent Maurer[1*], Emmanuel Gaucher[2], Marc Grunberg[3], Rike Koepke[2], Romain Pestourie[3] and Nicolas Cuenot[1]

*Correspondence: vincent.maurer@es.fr
[1] ES-Geothermie, 5 rue de Lisbonne, Le Belem, 67300 Schilitigheim, France
Full list of author information is available at the end of the article

Abstract

The development of the Rittershoffen deep geothermal field (Alsace, Upper Rhine Graben) between 2012 and 2014 induced unfelt seismicity with a local magnitude of less than 1.6. This seismicity occurred during two types of operations: (1) mud losses in the Muschelkalk formation during the drilling of both wells of the doublet and (2) thermal and hydraulic stimulations of the GRT-1 well. Seismicity was also observed 4 days after the main hydraulic stimulation, although no specific operation was performed. During chemical stimulation, however, no induced seismicity was detected. In the context of all field development operations and their injection parameters (flow rates, overpressures, volumes), we detail the occurrence or lack of seismicity, its magnitude distribution and its spatial distribution. The observations suggest the presence of the rock stress memory effect (Kaiser effect) of the geothermal reservoir as well as uncritically stressed zones connected to the GRT-1 well and/or rock cohesion. A reduction of the seismic rate concurrent with an increase of injectivity was noticed as well as the reactivation of a couple of faults, including the Rittershoffen fault, which was targeted by the wells. These results are derived from the homogeneous and consistent catalogue of more than 1300 local earthquakes that is provided. This reference catalogue is based on a standard detection method, whose output was manually verified and improved. The given absolute locations have been computed in a calibrated, geologically realistic 3D velocity model. Our work builds on previous analyses addressing the seismicity induced by the GRT-1 hydraulic stimulation and places the results into a historical context, thus considering the full dynamics of the observed phenomena. This paper also complements existing descriptions of the hydrothermal characteristics of the deep reservoir by providing insights separate from the wells.

Keywords: Seismic monitoring, Induced seismicity, Geothermal system, Stimulation, Upper Rhine Graben

Introduction

The Upper Rhine Graben (URG) currently hosts several enhanced geothermal system (EGS) plants that are in the exploitation phase, such as those in Rittershoffen and Soultz-sous-Forêts in France (Baujard et al. 2017; Genter et al. 2018), Landau and Insheim in Germany (Ganz et al. 2013; Küperkoch et al. 2018) and Riehen in Switzerland. Other EGS projects in France are in the drilling phase (Vendenheim and Illkirch-Graffenstaden) or

in an earlier stage (Eckbolsheim, Hurtigheim, Wissembourg), demonstrating the growing interest and viability in utilizing deep geothermal resources in the current energy mix. All of these EGS fields exploit hot local geothermal brine that is circulating in fracture and fault networks of Triassic sediments and the underlying granitic fractured basement. The geological context of this extensional basin hosts many faults bounding local horst and graben structures (Schumacher 2002), and the high geothermal gradient observed (Baillieux et al. 2013) strongly contributes to the geothermal development of this area.

EGS technology consists of increasing the low natural hydraulic performance of deep geothermal reservoirs by thermal, chemical and/or hydraulic stimulations. These stimulations aim to improve the connection of the wells with the nearby formation and increase the permeability in a reservoir, allowing the geothermal brine to be produced or reinjected at economically viable flow rates (Baujard et al. 2017; Nami et al. 2008; Portier et al. 2009; Schindler et al. 2010). In the course of these stimulations, seismicity is often induced (Majer et al. 2007; Zang et al. 2014), which, on the one hand, provides insight into the reservoir properties but, on the other hand, must be mitigated to prevent harmful effects on the population and goods, and on the project sustainability and acceptability (Deichmann and Giardini 2009; Gaucher et al. 2015). Seismicity can also be temporarily or continuously induced during the exploitation itself, i.e., during the inter-well circulation of the geothermal fluid (Baujard et al. 2018; Cuenot and Genter 2015; Evans et al. 2012; Megies and Wassermann 2014).

Worldwide, approximately 30 EGS sites have been or are being developed, and far fewer sites are active. This observation calls for continuous investigations of existing geothermal sites and an extensive description of any new site to increase the maturity level of such a technology, especially from a seismic risk perspective. Our work intends to contribute to this effort: we detail the occurrence or lack of seismicity, its magnitude distribution and its spatial distribution, in the light of all field operations and their injection parameters (flow rates, over-pressures, volumes). Thus, detailed description of the microseismic activity in parallel with the geothermal operations is presented for the first time for the Rittershoffen geothermal site. This paper complements the hydrothermal characterization of the Rittershoffen deep reservoir, performed by Baujard et al. (2017), and the seismicity analysis of Lengliné et al. (2017), by considering all reservoir operations, in addition to the hydraulic stimulation of the first well.

In this paper, first, we discuss the context of the Rittershoffen deep geothermal field. Then, the seismic networks implemented to monitor the field are described, as well as the processing, which was applied to the continuous records. Finally, the local seismicity identified during the major development phases (drillings, stimulations), which covers the period December 2012–June 2014, is characterized and discussed in the context of the field operational parameters.

Geothermal field context

Upper Rhine Graben geological setting

The deep geothermal field of Rittershoffen is located on the western margin of the NE–SW-striking central segment of the URG. The URG is a 300-km-long, 40-km-wide rift zone with an azimuthal extension averaging N20° E between Mainz (Germany) and Basel (Switzerland) (Fig. 1) (Ziegler 1992). It is associated with the Rhine valley, which is

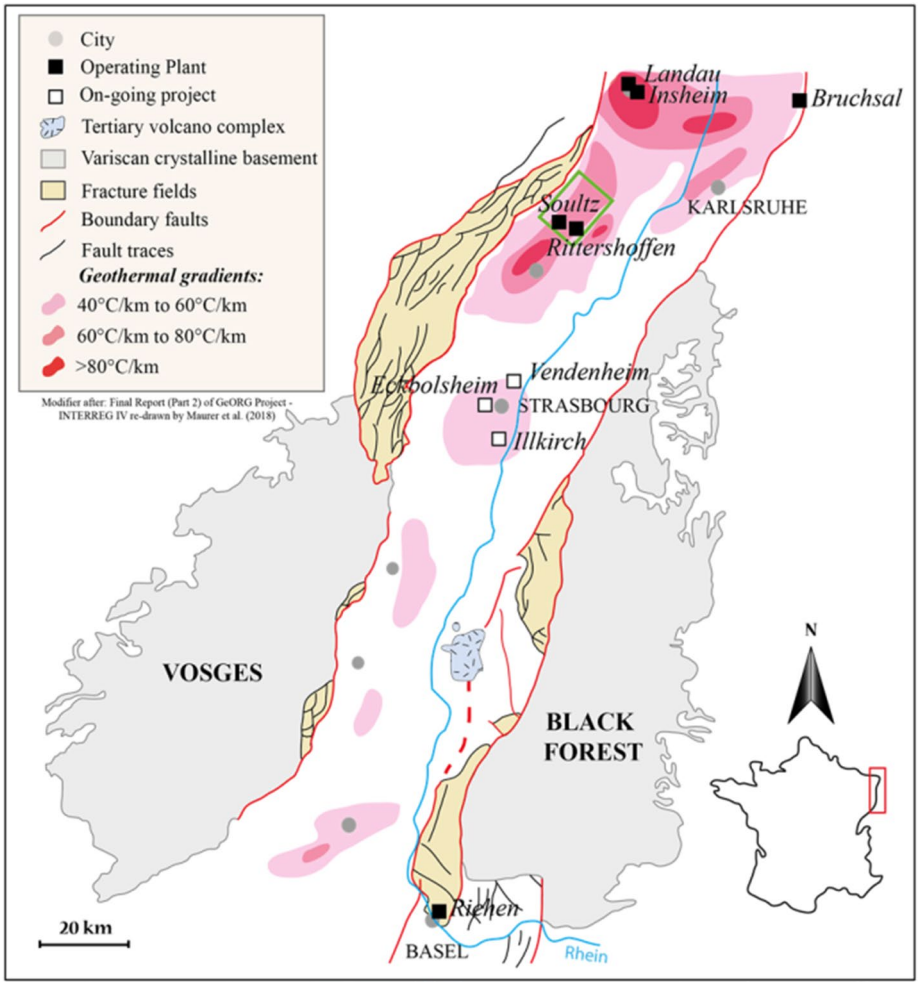

Fig. 1 Simplified geological map of the Upper Rhine Graben indicating the geothermal gradients and status of current deep geothermal fields (modified from the final report of the GeORG Project INTERREG IV 2013)

structurally bounded in the south by the folded Jura, in the west by the low-relief Vosges mountain range, in the east by the Black Forest massif and in the north by the Vogelsberg volcanic massif.

Tectonically, the western and the eastern edge of the URG are limited by major normal faults. A regional extension began 40 My ago, which is at the origin of the spacing between the Western and Eastern Rhine faults. Moreover, in the center of the graben, the sedimentological filling of the basin is syn-tectonic. The sedimentary cover is also affected by numerous normal faults, which also contributed to the opening of the URG.

Very favorable temperature gradients, higher than 60 °C/km, may be encountered at relatively shallow depths, and strong high-temperature anomalies also exist (Baillieux et al. 2013). Typically, from the surface to the top of the Middle Triassic (Muschelkalk), a conductive zone is observed, which is located above a multi-kilometric convective zone into which the geothermal fluid circulates (Fig. 2). The natural permeability in the convective zone is shown to be governed by the natural fracture system embedded in an approximately impermeable matrix (Baujard et al. 2017; Dezayes

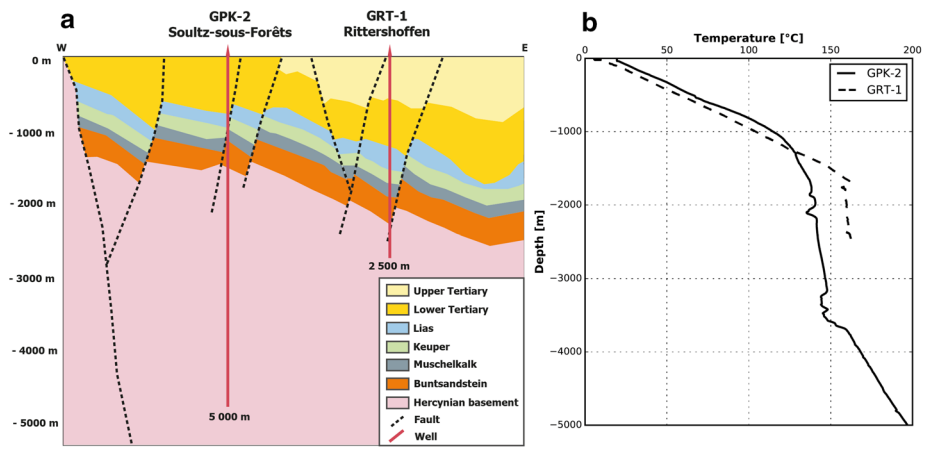

Fig. 2 **a** East–West simplified vertical section of the Rhine Graben crossing the Soultz-sous-Forêts GPK–2 and the Rittershoffen GRT-1 wells (from Edel et al. 2018); **b** temperature logs, at equilibrated thermal conditions, for the Soultz-sous-Forêts GPK-2 well (from Genter et al. 2010) and for the Rittershoffen GRT-1 well (from Baujard et al. 2017) (vertical scale is in MD)

et al. 2010; Genter et al. 2010; Sanjuan et al. 2016). Consequently, natural faults play a major role in geothermal reservoir circulation and are the primary targets for exploitation. Therefore, almost all projects in the URG exploit the deep, fractured reservoirs located within the Triassic sediments and/or the crystalline basement (Soultz-sous-Forêts, Landau, Insheim, Rittershoffen) (Fig. 2).

Rittershoffen geothermal site development

Rittershoffen is located in northern Alsace, ~7 km southeast of Soultz-sous-Forêts. Designed for direct use of geothermal heat, the deep geothermal plant of Rittershoffen is one of very few plants of that kind currently operating in Europe. The plant currently produces a thermal power of 24 MWth, with a production temperature of 170 °C and a production flow rate of 70 L/s. The geothermal heat is provided to a biorefinery located in the city of Beinheim, 15 km away from the geothermal plant, through a specific transport loop.

The historic exploitation of oil and gas in the area highlighted the high-temperature anomalies at the Rittershoffen site. Furthermore, the reprocessing of 2D vintage seismic reflection profiles provided a preliminary structural model of the subsurface and revealed a major fault that affects the entire sedimentary cover and propagates into the granitic basement at a relatively shallow depth (~2.2 km below surface). Accordingly, Rittershoffen was selected for the development of a geothermal site and the Rittershoffen normal fault selected as target for the geothermal wells.

The first well, GRT-1, reached a final measured depth (MD) of 2580 m at the end of December 2012 (Fig. 3). Its open-hole section crosses the Buntsandstein sandstone and the fractured Paleozoic granite (Duringer et al. in press). Various logs and hydraulic tests were performed throughout the year 2013. Because the initial well injectivity index was low, a strategy was defined to enhance the connection of the well to the reservoir and the fracture system. Stimulation operations were applied in two

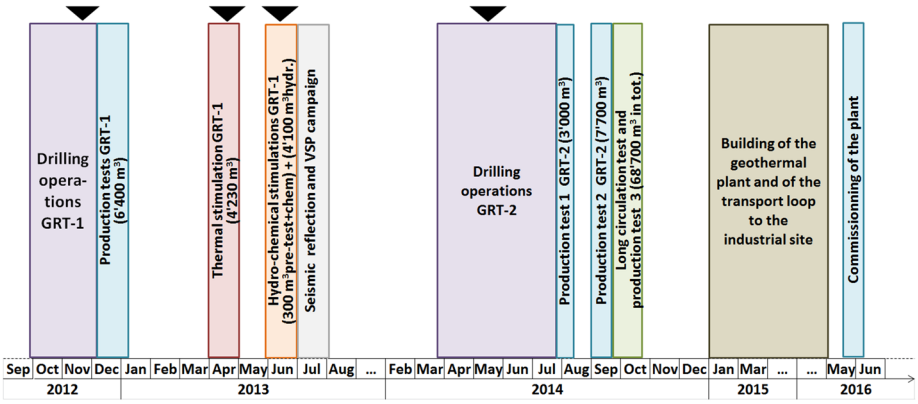

Fig. 3 Timeline of the operations performed during the development of the Rittershoffen deep geothermal field. The seismogenic periods of interest (during GRT-1 drilling, thermal and hydraulic stimulations and GRT-2 drilling) are indicated by black triangles

sequences: first in April 2013, with a thermal stimulation and, second in June 2013, with both chemical and hydraulic stimulations.

The injection temperature being similar in thermal and hydraulic stimulations (about 10 °C), the main difference lies in the injection flow rate. In a thermal stimulation, fluid injection is performed under reduced flow rate, which is expected to predominantly activate thermo-mechanical effects to enhance the reservoir permeability. On the contrary, higher flow rates are applied during hydraulic stimulation to activate hydro-mechanical effects.

After successful stimulation, which increased the initial injectivity index by a factor of five (Baujard et al. 2017), an active 2D seismic survey was performed. The main purpose was to define the trajectory of the second well of the doublet, GRT-2, and to improve the structural model of the underground (see subsection "Velocity model"). Thus, the drilling of GRT-2 started in March 2014 and ended in August 2014. GRT-2 is a deviated well, 3200 m in length, that reaches 2707 m TVD GL.

Production and circulation tests were performed after the drilling phase. No reservoir enhancement was necessary because production tests revealed that the initial productivity index was high enough, between 2.8 and 3.5 L/s/bar for the expected exploitation flow rate (Baujard et al. 2017). The year 2015 was dedicated to constructing the heat transport loop and the geothermal plant, which was commissioned in May 2016 and has been continuously operating since.

Six months prior to any field operation, seismicity was monitored by several networks (see subsection "Seismic monitoring"). No seismicity (natural or induced) was detected during this period. Four main seismogenic periods were later identified (Maurer et al. 2015): first, during the drilling of the first well, GRT-1; second, during the thermal stimulation of GRT-1; third, during the hydraulic stimulation; and fourth, during the drilling of GRT-2. This paper focuses on these four seismogenic periods.

Velocity model

In such a geological context, using a 1D velocity model is not the best method to accurately locate the seismicity induced at the Rittershoffen site. Moreover, the fault

identified as the most permeable zone in the area and targeted by the geothermal doublet exhibits ~ 350-m offset (~ 200-m vertically). Accordingly, a 3D velocity model was developed for the area. This model is based on the active seismic interpretation and the geological and geophysical logs acquired in GRT-1.

First, the numerous vintage seismic lines were reprocessed to better represent the deep formations. Following the June 2013 active seismic survey, two seismic lines, centered on Rittershoffen and oriented NNW–SSE and W–E, were added to the 3D seismic processing flow. Hence, five main seismic horizons were identified: the top of the "Fish shale" (Oligocene top), the top of the Lias (Jurassic top), the marl–calcareous lithological transition (Keuper or Trias top), the calcareous–sandstone lithological transition (top of the Buntsandstein) and the altered crystalline basement (top of the basement). In addition to the horizon selection, many faults were identified and incorporated for interpretation. Time-to-depth conversion of the horizons was constrained using vertical seismic profiles (VSPs), available sonic logs or check-shots. In the Rittershoffen zone, only the VSP data associated with the GRT-1 well were available and thus used. The five main horizons could be accurately positioned in depth at and around the GRT-1 well. With this active seismic interpretation, a regional model covering ~ 250 km^2 was obtained (Maurer et al. 2016).

In the second step, the VSP, the sonic log and the stratigraphic interpretation of GRT-1 (Aichholzer et al. 2016; Duringer et al. in press) were compared to better constrain the velocity model near GRT-1. As a result, two interfaces exhibiting noticeable velocity contrasts were added to the five main seismic interfaces. One corresponds to the bottom of the weathered zone, positioned 80 m below the surface. Its topography was assumed to follow the ground surface topography. The second interface corresponds to the top of the Muschelkalk formation, which is located between the Keuper and Buntsandstein formations. The top of the Buntsandstein surface was considered to be representative of the top of the Muschelkalk formation.

Once the underground layers were defined, the VSP data were used again to compute P-wave interval velocities (Vp) for each formation. Although the velocity is computed along GRT-1, it is assumed to be representative of the entire Rittershoffen area.

To develop the S-wave velocity (Vs) model, the full sonic log was used. From this log, average Vp/Vs ratios were calculated for the identified layers, thus providing interval S-wave velocities. Because the full sonic log was acquired below ~ 450 m MD, the Vp/Vs ratio was fixed to 2.12 for the two shallowest formations, i.e., until the top of the "Fish shale". This ratio corresponds to the median value measured at the top of the "Fish shales".

The final Vp, Vs and Vp/Vs values for each formation of the final 3D model are provided in Table 1. Figure 4 shows the corresponding profiles along GRT-1 with the entire sonic log. As observed, the P-wave velocity derived from the VSP (red curve) is consistent with the P-wave velocity derived from the full sonic log (dark gray curve). Furthermore, the main interfaces considered in the final model correspond to noticeable velocity contrasts in the sonic log. Figure 4 also shows as background a vertical South–North section of the 3D P-wave velocity model, next to GRT-1 and GRT-2 wells (red curves).

Table 1 Interval seismic velocities applied in the 3D velocity model

Interface	Depth in GRT1 (m TVD MSL)	Vp (m/s)	Vs (m/s)	Vp/Vs
Surface (at GRT1)	− 151	1300	613	2.12
Bottom of weathered zone	− 71	2315	1092	2.12
Top of "Fish shales"	272	2961	1544	1.92
Top of Lias	1023	3332	1778	1.87
Top of Keuper	1298	4307	2413	1.78
Top of Muschelkalk	1504	5236	2821	1.86
Top of Buntsandstein	1649	4818	2858	1.69
Top of unaltered granite	2209	5951	3351	1.78

The velocity parameters apply below the depth of the mentioned interfaces, which is given along GRT1

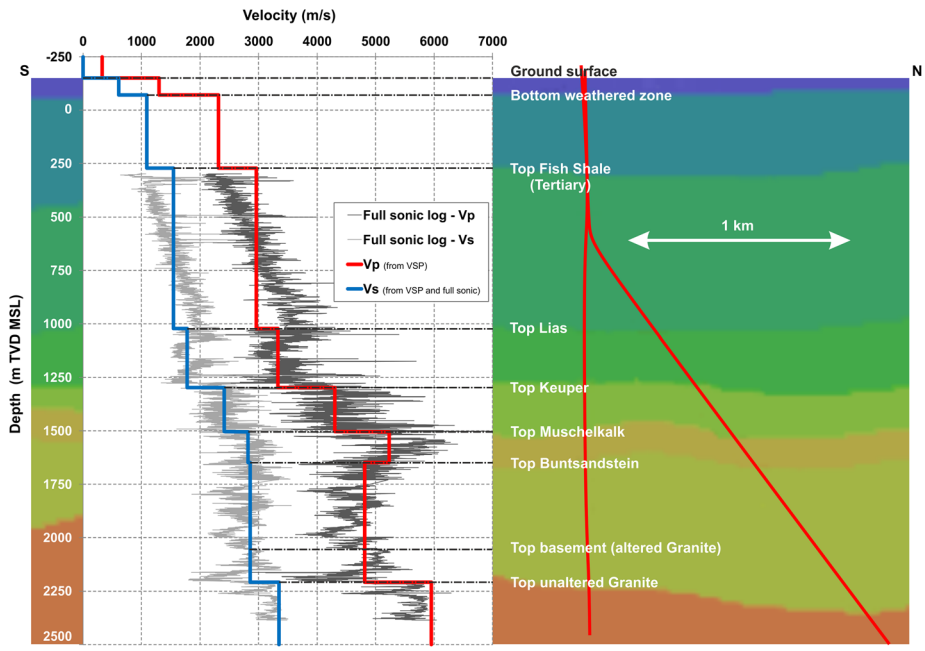

Fig. 4 Vertical profile of the 3D velocity model along GRT-1 overlaying a vertical South–North section of the 3D P-wave velocity model next to GRT-1 and GRT-2 wells (red curves). The red velocity profile indicates the Vp derived from the VSP, the blue velocity profile indicates the Vs derived from the VSP and the Vp/Vs ratio of the full sonic (see text for further explanations). The Vp and Vs measured by the full sonic log are presented for comparison in dark and light gray, respectively

To locate induced seismicity, this 3D velocity model is discretized with a 20-m side cubic mesh.

Seismic monitoring

Permanent monitoring network

To detect any seismicity induced by the Rittershoffen field operations, a permanent seismic network, of four surface stations, was deployed 6 months before any drilling operation, which was in compliance with the French mining authorities. This network completed the eastern part of the network dedicated to the surveillance of the Soultz-sous-Forêts geothermal plant, composed of eight surface stations in operation since

2002. Thus, since 2012, the micro-seismic activity of the Rittershoffen geothermal project has been monitored by a permanent seismic network of 12 surface stations (Fig. 5).

The Soultz-sous-Forêts network is composed of 1-Hz short-period seismometers, consisting of one or three components (L4C/L4C-3D), deployed at the surface. Signals are digitized on site, sampled at 150 Hz and transmitted to a central site. At the central site, a SeisComp3 (Hanka et al. 2010) plugin enables the *École et Observatoire des Sciences de la Terre* of the University of Strasbourg (EOST) to get the data in real-time via an internet connection. The Rittershoffen network is also composed of 1-Hz, short-period, three-component seismometers (L4C-3D) deployed at the surface. The signals were initially digitized at a sampling rate of 100 Hz that was increased to 200 Hz beginning of 2014. The digital data are sent in real-time to a central site where a SeisComp3 server allows EOST to access them via an internet connection.

This permanent seismic network was the only one actively monitoring prior to the chemical and hydraulic stimulation of GRT-1 in June 2013 (Fig. 5 and Table 4).

Temporary monitoring network

In addition to the permanent network, several temporary surface stations were deployed in June 2013, using equipment belonging to the Geophysical Instrument Pool Potsdam

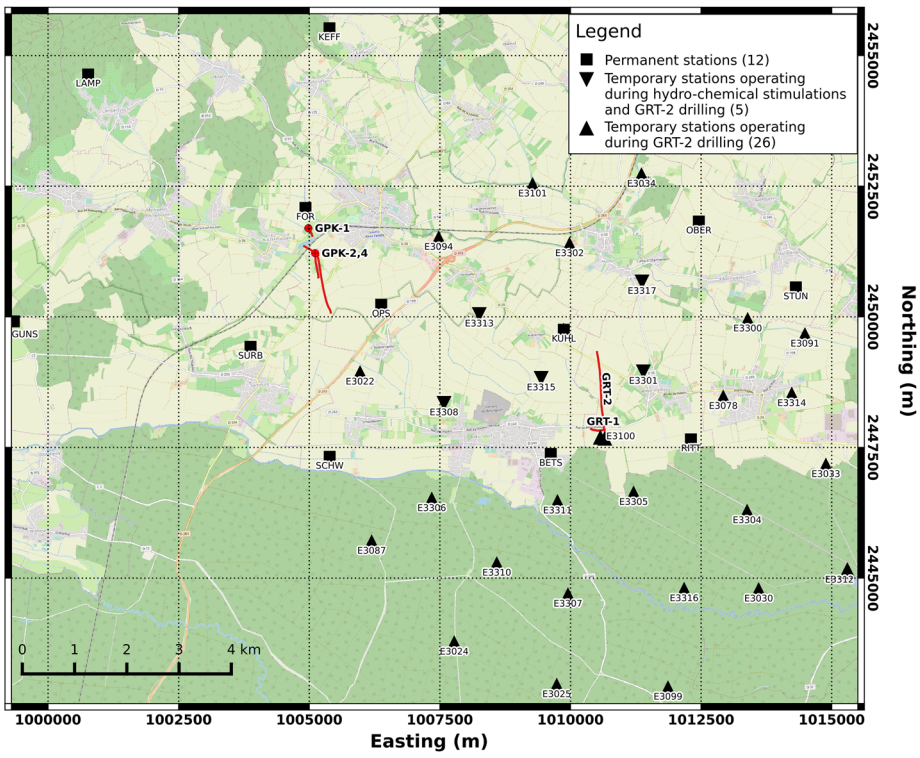

Fig. 5 Map of the location of the 43 seismological stations monitoring the Rittershoffen geothermal field. The 12 permanent stations are indicated with black squares; these were active during all development operations. The five temporary stations recording from the start of GRT-1 chemical and hydraulic stimulation are displayed as black inversed triangles. The 26 temporary stations added before GRT-2 drilling commenced are displayed as black triangles. The trajectories of the Rittershoffen and Soultz-sous-Forêts geothermal wells are also indicated in red

(GIPP) of the GFZ German Research Centre for Geosciences (Gaucher et al. 2018). The primary objective was to improve the detection and location capabilities of the seismic monitoring during the field development operation (i.e., well tests; chemical and hydraulic stimulations of GRT-1; drilling, stimulation, and production tests of GRT-2; and further circulation tests). A secondary objective was to apply and test several processing techniques based on dense seismic networks (Gaucher et al. 2013). Hence, a dense network lay-out was designed as a large antenna focusing on the geothermal wells and providing homogeneous coverage. It consisted of three circles centered on the wellheads with radius up to 5 km (i.e., about twice the depth of the geothermal reservoir) and a distance between the stations ranging between 1.5 and 2 km. Consequently, 31 three-component seismometers were added temporarily to the permanent network. Short-period, 1-Hz seismometers (L4C-3D) were selected because microseismicity was the main focus. The signals were digitized, sampled at 300 Hz and stored as miniSEED files. Several stations periodically uploaded the files to the SeisComp3 server at EOST, thus providing shortly delayed seismograms complementing the permanent network data.

During the chemical and hydraulic stimulations of GRT-1—the third seismogenic phase of the project (June 2013)—a total of 17 seismic stations (12 permanent, five temporary) were monitoring (Fig. 5 and Table 4). From April to November 2014—the fourth and final seismogenic phase of the project—all temporary stations were operational and recording. Thus, during that period, which includes the GRT-2 drilling, 43 stations were continuously monitoring the area.

Figure 5 shows the location of all seismic stations constituting the monitoring network installed between 2012 and 2014 around the Rittershoffen geothermal field. The dense part of the network centered around GRT-1 and GRT-2 is clearly visible as well as the relatively regular spacing between the stations. The periods during which the stations were active are also indicated in Table 4: Appendix provides the exact location of the stations and their operational periods.

Data processing

During real-time monitoring, the SeisComp3 automatic detection parameters were changed over time, as knowledge was gained from the identified seismicity. These changes led to inhomogeneous detection capabilities hence an inconsistent seismological catalogue over time. To correct from this bias, all continuous waveforms acquired around the seismogenic periods were processed again using a homogeneous automatic detection procedure based on the SeisComp3 toolbox. This detection procedure combined the grid-search method of the "scautoloc" module with the density-based clustering algorithm (Ester et al. 1996) of the "scanloc" module (Clinton et al. 2018; Grigoli et al. 2017). The latter can use S-picks and performs generally better than the former. The scanloc detection parameters were tuned using a parameter sweep method, on an initial database that contained all induced earthquakes identified by manual and systematic review of the data recorded during the first 6 h of the GRT-1 hydraulic stimulation. The recovery rate of the final automatic system applied to this initial database reached 96%. This re-processing stage guarantees homogeneous detection capabilities over the period of interest. Once applied, all events detected automatically were manually controlled. For the local earthquakes, correction or addition of the P- and S-wave onset

times with the associated uncertainties was done and, when possible, the peak-to-peak amplitude of the P-wave on the vertical component and the associated half-period were measured. Then, the earthquakes were located in the 3D velocity model (see subsection "Velocity model") using the NonLinLoc software (Lomax et al. 2000, 2009; Lomax 2018) with the application of the Bayesian inversion approach proposed by Tarantola and Valette (1982) and the oct-tree importance sampling algorithm (Lomax and Curtis 2001). The location provides the earthquake hypocenter together with its uncertainty given as a 3D uncertainty ellipsoid (Lomax 2018). For simplicity, in the following, the location uncertainty will be quantified by one parameter only: the largest half-length of the major axis of the uncertainty ellipsoid.

Although the velocity model is relatively well defined from prior data, a major source of location error still lies in the S-wave velocity value of the superficial layers (see subsection "Velocity model"). To decrease the impact of such an unknown and to increase the hypocenter accuracy, the velocity model was calibrated using a seismic event recorded while drilling the GRT-2 well. On May 26, 2014, the drill bit became stuck in the GRT-2 at a depth of 1862 m MD (the total depth was 2123 m MD at that time), in the Middle Muschelkalk formation (Trias). During one of the attempts to free the bottom-hole assembly, the mud pressure increased, resulting in mud losses and induced seismicity. Interestingly, the drilling of this well section was performed with a rate of penetration that was higher than in the previous and next depth intervals, which supports the existence of a weak or fractured zone at this depth and could well explain the adherence of the bottom-hole assembly and the subsequent mud losses and induced seismicity. Consequently, we can reasonably assume that the initial seismicity occurred at the well at that depth. Hence, one of the first recorded earthquakes associated with this incident was positioned at 1862 m MD in GRT-2 and used as a "calibration shot" (event 2014-05-26T13:33:24.622974Z). This event was chosen because 73 seismic phases were picked, among which were 38 P-waves; thus, both phases were observed on almost all 43 stations of the network. The event location was determined using the 3D velocity model and only the P-wave arrivals to avoid contamination from the unconstrained S-wave velocity in the first 450 m of the model and because the network coverage at that time was sufficiently homogeneous. Hence, the earthquake origin time could be estimated and used to compute the observed travel times of both P- and S-waves to the seismic stations. After subtracting the latter from the theoretical travel times computed between the 1862 m MD reference point in GRT-2 and the stations, time differences at each station for both phase types were obtained. By adding the time differences to the corresponding observed wave arrivals, the calibration shot could be perfectly relocated to its expected position. Finally, such a time correction was systematically applied to the picked arrival times prior to locating any identified earthquake and compensates, to a certain extent, for the inadequacy of the 3D velocity model in the superficial layers.

Once the earthquake hypocenter was obtained, the magnitude determined at the station KUHL was assigned to the earthquake. Usually, the event magnitude is estimated from the average magnitude obtained at the different stations of the network. However, this procedure was not applied for three reasons. First, the coverage and the number of stations of the seismological network changed over time, which would lead to changing average magnitude for a similar event. Second, the KUHL station is a permanent

station that was operating during all seismogenic periods. It is located approximately 2.5 km NNW from the well pad (Fig. 5) and shows a good signal-to-noise ratio around the P-wave arrival, also for weak events. Therefore, a local magnitude at this station could be estimated for 95% of the located earthquakes, which was not the case for any other station of the network. Finally, the seismic focal mechanisms inverted for the different seismogenic periods (see subsection "Spatial distribution") show similar rupture geometry when the latter is well determined, or, at least, consistent polarities at the measured stations, when many solutions may fit. So, the radiation coefficient to station KUHL may be considered relatively constant over time. Consequently, the magnitude determined at the single permanent station KUHL is the most consistent over time and will allow comparisons between the four seismogenic periods. (When the P-wave amplitude could be measured at a station different from KUHL, its associated magnitude was computed. This showed that, on average, the difference in magnitude between the KUHL station and the other station remained consistent for all processed events.) To calculate the magnitude, the formula of Bakun and Joyner (1984) was applied using their default parameters. The approach using the P-wave peak-to-peak amplitude and the corresponding half-period, measured on the vertical component of KUHL, was selected because it is less sensitive to high low-frequency noise that may contaminate a weaker higher-frequency seismic arrival. This is particularly noticeable for small magnitude local earthquakes, for which magnitude determination is always critical (Kendall et al. 2019).

To estimate the magnitude of completeness of the seismic catalogue, or part of it, and the *b*-value for the corresponding earthquake set, we applied the goodness-of-fit approach, as described by Wiemer and Wyss (2000) and Aki (1965), which assumes that the frequency–magnitude distribution of the seismic events follows a Gutenberg–Richter power law (see subsection "Magnitude distribution").

Results

The processing procedure was applied to the continuous seismic data recorded during and around all major development operations: GRT-1 drilling, stimulations and testing; and GRT-2 drilling (Fig. 3). The result is a reference seismic catalogue, which is available as Additional file 1. Geographical coordinates are given in "Lambert II étendu" and the reference selected for depths is the mean sea level (MSL). The altitude of the geothermal platform is 149 m. This catalogue is more exhaustive and consistent than the preliminary catalogue presented by Maurer et al. (2015).

Table 2 summarizes the characteristics of the observed seismicity in parallel with the primary characteristics of the reservoir development operations.

In total, 1348 earthquakes were detected: 26 during GRT-1 drilling, 146 during GRT-1 thermal stimulation, 992 during hydraulic stimulation of the same well and 184 during GRT-2 drilling. Thus, the hydraulic stimulation of GRT-1 was the most seismogenic operation.

The local magnitude of the seismicity ranged between −1.5 and 1.6 and the magnitude of completeness was estimated to be between −0.65 and 0.05 (see next subsections for details). None of the induced events was felt by the population.

Table 2 Summary of the seismicity observed during the development of the Rittershoffen geothermal reservoir

First event Last event	N_{EVT}	M_{MIN} to M_{MAX}	ΔDepth (m TVD MSL)	Q_{MAX} (L/s)	WHP_{MAX} (MPa)	Volume (m^3)	Duration (h)	Productivity and injectivity indices (L/s/bar)
Drilling of GRT-1								
2012-11-29T22:23:33 2012-11-29T22:51:42	26	− 1.3 to 0.6	1200–2000	–	–	–	–	$P = 0.45$
GRT-1 production test								
None	–	–	–	–	–	6400	216	$P = 0.6$
Thermal stimulation of GRT-1								
2013-04-24T07:24:05 2013-04-25T09:44:28	146	− 1.5 to 0.3	1300–3050	25	2.8	4135	62.6	$I = 0.9$
Pre-stimulation test and chemical stimulation of GRT-1								
None	–	–	–	27 + 5	2.5 +/	357 + 269	6.5 + 14.2	$I = 1.7$
Hydraulic stimulation of GRT-1 and injection test								
2013-06-27T15:23:38 2013-07-01T00:19:11	831	− 1.4 to 0.9	1200–2000	80 + 60	3.3 + 2.2	3180 + 820	21.7 + 6.5	$I = 2.5$
2013-07-02T04:46:15 2013-07-12T22:14:23	161	− 0.9 to 1.6	1300–2050	–	–	–	–	–
Drilling of GRT-2								
2014-05-26T12:18:06 2014-05-26T23:43:55	184	− 1.5 to 1.0	1250–1850	–	–	–	–	$P = 2.8$ to 3.5

For each period, N_{EVT} represents the number of located events, M_{MIN} and M_{MAX} are the minimum and maximum observed magnitudes, respectively, and ΔDepth is the depth interval containing 80% of the events. Finally, Q_{MAX}, WHP_{MAX}, Volume and Duration correspond to the maximum flow rate, maximum wellhead pressure, total injected or produced volume and duration of the stimulation operations, respectively. The productivity or injectivity indices have been measured following the associated operations

In the following subsections, the seismicity, which was recorded during GRT-1 drilling, GRT-1 thermal, chemical and hydraulic stimulations and during GRT-2 drilling is described in greater detail. Interpretation of these results and comparison of the seismogenic behaviors between these different phases is presented in the "Discussion" section.

Seismicity during GRT-1 and GRT-2 drilling

During the drilling of the GRT-1 well, seismicity was induced and was most likely due to circulation losses while setting the 9–5/8″ pipe in the 12″1/4 open-hole section, between 1029 and 1773 m TVD MSL. The mud parameters had a flow rate of 17 L/s and an injection pressure of 4.8 to 6 MPa. A total of 26 earthquakes were recorded on November 29, 2012, within a period of 30 min (between 22:23 and 22:51 UTC). The magnitude ranged between − 1.3 and 0.6.

Figure 6 shows the location of these events. As observed, the hypocenters are generally oriented in a South–North direction. However, as emphasized by the depth sections,

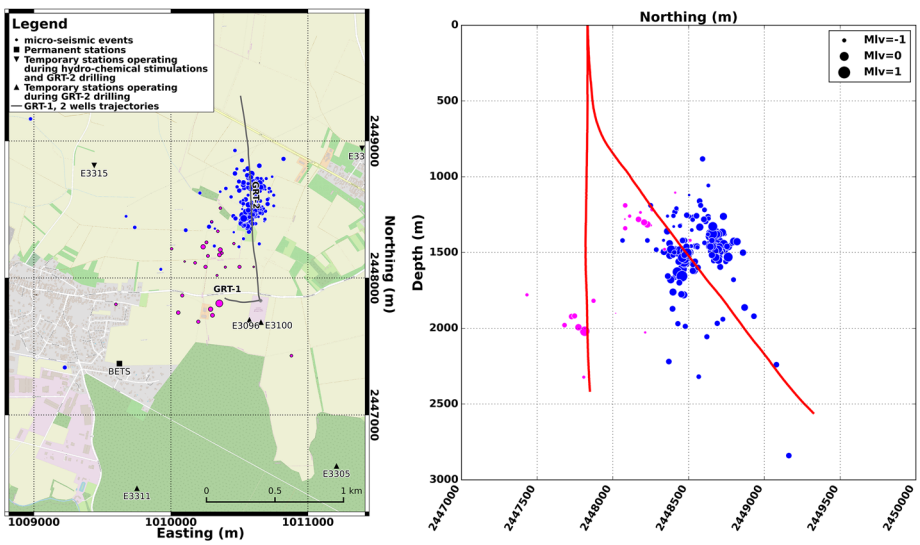

Fig. 6 Epicenter map (left) and South–North vertical projection (right) of the seismicity recorded during the GRT-1 drilling (magenta circles) and GRT-2 drilling (blue circles)

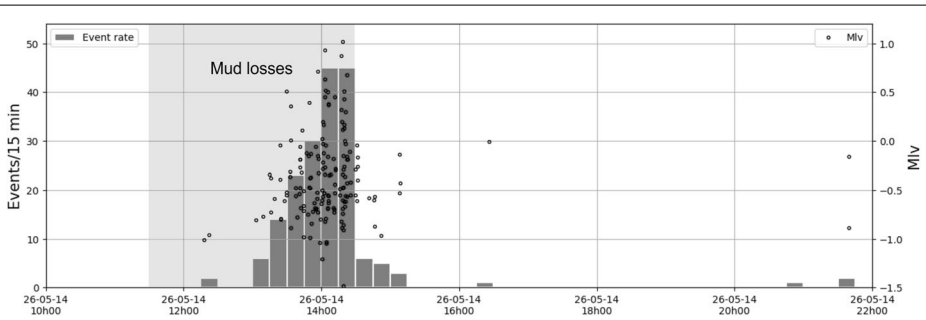

Fig. 7 GRT-2 drilling. Seismic rate, per 15 min, and local magnitudes of the recorded earthquakes

they are divided into two clusters: a northern one between 1200 and 1400 m and a southern one between 1800 and 2000 m that is near GRT-1. The low number of events and their weak magnitudes prevent a reliable interpretation of the associated hypocenters. Furthermore, the network configuration may bias the results as explained in the subsection "Spatial distribution" of "Discussion".

As previously mentioned (see section "Data processing"), earthquakes were also induced on May 26, 2014 during GRT-2 drilling operations (Fig. 7). A total of 184 earthquakes were detected, 177 within 3 h (between 13:00 and 16:00 UTC) (Fig. 7. However, most of the seismicity occurred within approximately 1 h, between 13:30 and 14:30 UTC). The maximum seismic rate was 45 events in 15 min. The magnitude range of these local earthquakes was between − 1.5 and 1.

As observed in Fig. 6, the first hypocenters are centered on GRT-2 at the depth of the mud losses (1517 m TVD MSL), as expected from the location calibration procedure (see subsection "Data processing"). However, the seismicity later divided into two clusters, about 200 m apart, one to the south and one to the north of the well. They are

aligned in a N7° E direction and both are approximately at the same depth interval in the Muschelkalk. During GRT-2 drilling, 80% of the hypocenters exhibited uncertainties between ±20 m and ±200 m, with a median of ±55 m. Therefore, the location uncertainties cannot affect the observation of the two clusters that may be associated with real geological features.

Seismicity during GRT-1 thermal stimulation

The first significant induced seismicity occurred during GRT-1 thermal stimulation in April 2013, which was 4 months after drilling (Fig. 8). A total of 146 induced earthquakes were detected and located. The stimulation consisted of injecting reservoir fluids, previously discharged from GRT-1, at an ambient temperature of 10 °C into the open-hole section of the well (1773 to 2431 m TVD MSL) that was drilled into sandstone and granite (silicate rocks), which had a temperature of approximately 160 °C. Thus, between April 23 and 25, 2013, over the course of 62.6 h, 4135 m^3 of brine were injected. The initial injection flow rate of 10 L/s was increased stepwise by 5 L/s, up to 25 L/s, and then decreased stepwise to 15 L/s before ending. The wellhead pressure (WHP) quickly increased to 2.8 MPa at 15 L/s; the pressure subsequently remained below that level but was generally above 1.8 MPa, regardless of the injection rate. No downhole pressure gauge was available during GRT-1 thermal stimulation.

The first detected induced event occurred 26 h after the beginning of the injection. Considering the WHP, this event occurred 21 h after a first raise of the WHP to the maximum value of 2.8 MPa, at 15 L/s, or 3 h after the WHP reached its maximum value again at 20 L/s. However, the majority of the seismic activity occurred 39 h after the start of injection, when the flow rate reached 20 L/s, then 25 L/s, with a maximum rate of approximately one event per minute. Interestingly, the seismic rate decreased strongly while the injection was on-going at 25 L/s, whereas the WHP decreased from 2.7 to 2.2 MPa. A last burst of seismicity was observed at 25 L/s (1.9 MPa). These events occurred 4 h before the decrease of the injection rate from 25 to 20 L/s or 11 h before the injection was stopped.

In total, 146 events were detected and located, with magnitudes ranging from −1.5 to 0.3. Most of the seismicity occurred between 22:00 and 06:00 local time, which explains the ability of the system to detect small magnitude earthquakes, as low as Mlv = −1.5.

As presented in Fig. 8, most of the earthquakes are clustered around and north of the GRT-1 well. After removal of the outliers, the best plane fitting the hypocenter distribution (least-squares criterion) has a N3° E direction, dipping 86° W. The length of the primary cloud is ~1500 m along its main direction and is ~500 m wide. Eighty percent (between the 10th and 90th percentiles) of the hypocenters are located between 1300 and 3050 m depth (the deepest events are not visible in Fig. 8) and have location uncertainties between ±80 m and ±250 m, with a median of ±135 m. The shallowest events are the northernmost and the deepest are the southernmost. Deeper and to the south of the primary seismic cloud, earthquakes along the main direction are observed.

Seismicity during GRT-1 chemical and hydraulic stimulations

In June 2013, additional stimulations were performed in GRT-1 (Fig. 9). Following a pre-stimulation test on June 22, chemical treatments of three different sections of the open-hole isolated by packers were performed on June 23, 24 and 25. In total, 269 m^3

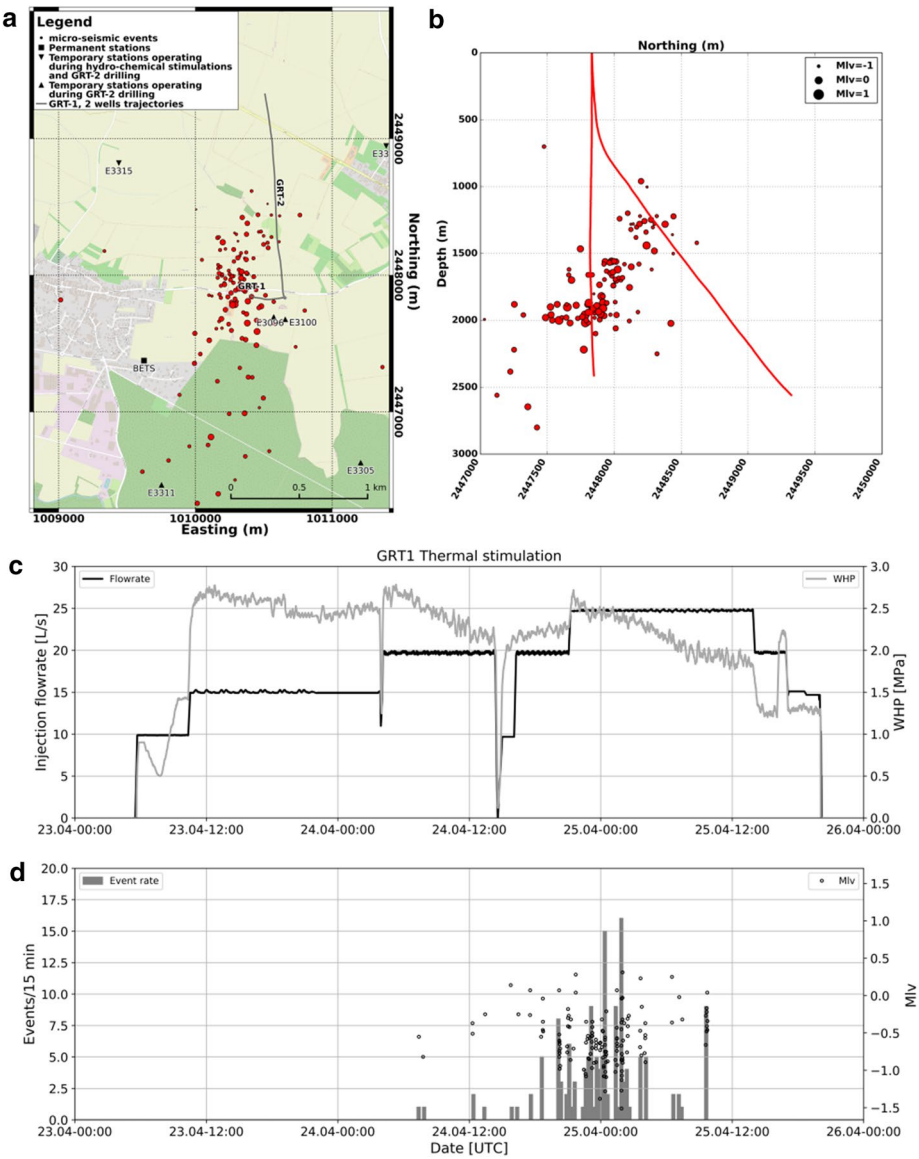

Fig. 8 GRT-1 thermal stimulation: epicenter map (**a**) and South–North vertical projection (**b**) of the seismicity recorded (red circles); injection flow rate and wellhead pressure over time (**c**) in parallel with the seismic rate per 15 min and the local magnitude (**d**)

of fluid, of which 216 m^3 were biodegradable acids, were injected (Baujard et al. 2017). No seismic activity was detected during these operations (Fig. 9).

On June 27 and 28, 2013, hydraulic stimulation of the GRT-1 open-hole section was performed, followed by a short injection test (Fig. 10). During hydraulic stimulation, the injection flow rate was raised stepwise from 5 to 80 L/s and then decreased stepwise. Approximately 3180 m^3 of brine were injected within approximately 21.7 h. The maximum WHP was 3.3 MPa, and the maximum downhole overpressure (DHP) was 3.0 MPa, both of which were reached at the end of the highest injection rate period (80 L/s). During the post-stimulation test, 820 m^3 of brine were injected at a specified flow rate, which was also increased stepwise up to 60 L/s and then decreased

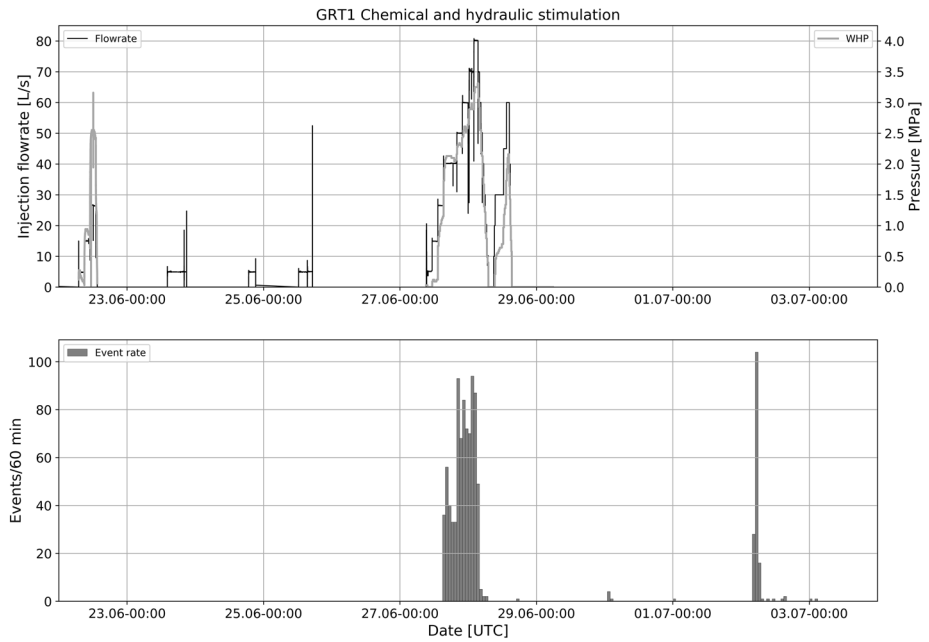

Fig. 9 GRT-1 pre-stimulation test, chemical and hydraulic stimulations. Injection flow rate and wellhead pressure (top) in parallel with the seismic rate per hour and local magnitude (bottom)

stepwise. The post-stimulation test began 2 h after the hydraulic stimulation for a total duration of approximately 6.5 h. The maximum WHP and DHP were both equal to 2.2 MPa.

In total, 824 earthquakes were detected and located during the hydraulic stimulation. The seismic activity began 6 h after injection began, when the flow rate changed from 26.5 to 40 L/s and the WHP reached 1.5 MPa (DHP = 1.8 MPa). Then, seismicity occurred continuously with an increase of the seismic rate. Starting with an average of 40 events per hour, the rate reached an average of 80 events per hour. The maximum observed rate was 50 events per 15 min, which was observed at the time the flow rate increased from 40 to 50 L/s and the WHP reached 2.2 MPa (DHP = 2.4 MPa). Seismicity observed during the injection for the most part stopped during the injection step down, when the rate was back to 50 L/s and WHP = 2.2 MPa (DHP = 2.4 MPa), i.e., 2.5 h before injection stopped. The magnitude of the observed events ranged between − 1.4 and 0.9, and the largest event occurred during the time of the highest injection rate of 80 L/s.

During the short injection test, no seismicity was recorded, even if the flow rate was raised as high as 60 L/s with a WHP = 2.2 MPa (DHP = 2.4 MPa). However, one event was recorded 1.5 h later.

In addition to the six earthquakes recorded on the June 30 and July 1, 2 days after injection (34 h), the most striking observation was a burst of seismicity on July 2, 4 days after injection (425 h) and in the absence of any on-site operation (Fig. 10). Within approximately 1.5 h, 146 earthquakes were recorded with a magnitude range between − 0.9 and 1.6.

The earthquakes observed during the hydraulic stimulation were located around GRT-1 and extended to the north (Fig. 10). The cloud they formed was approximately

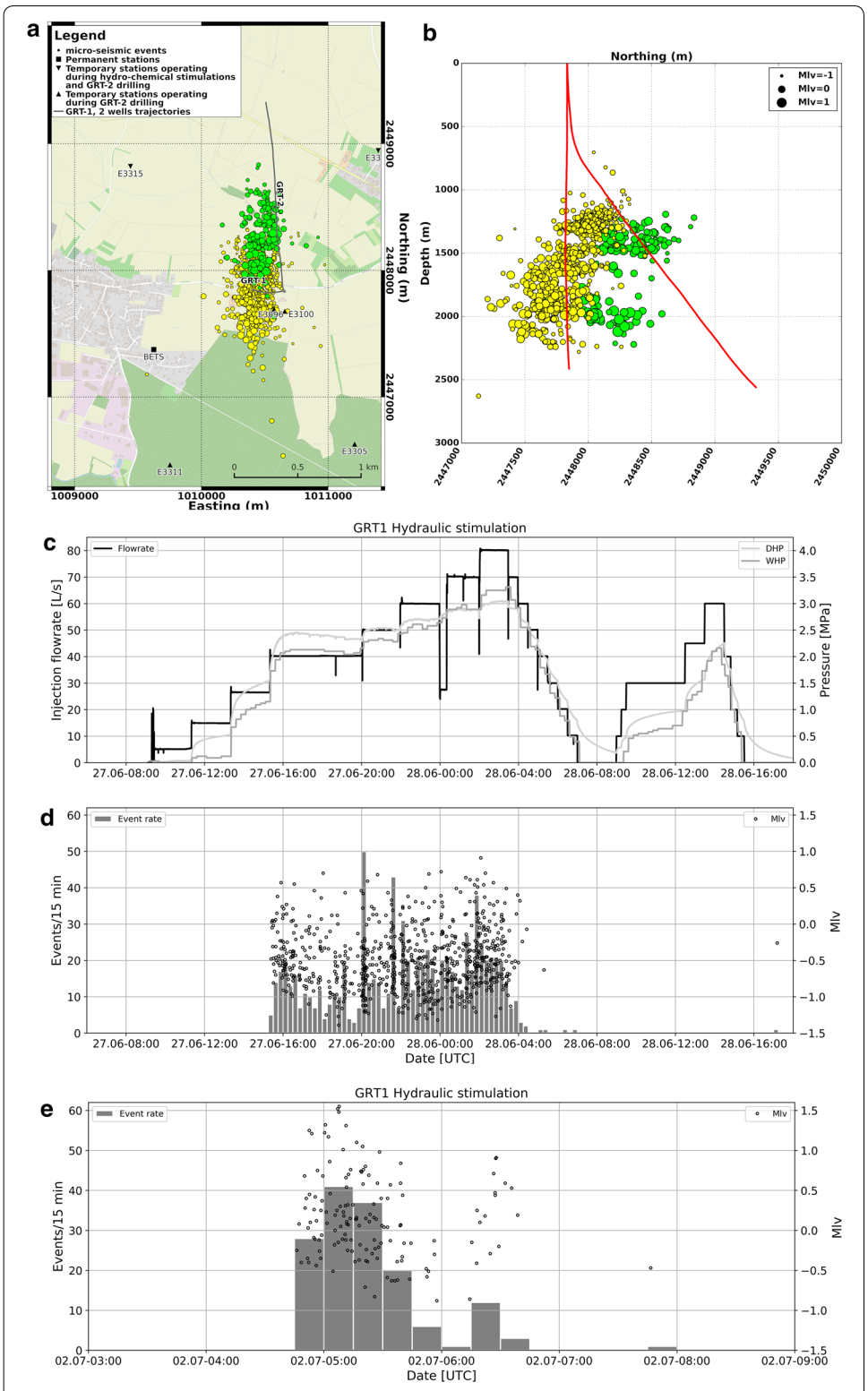

Fig. 10 GRT-1 hydraulic stimulation: epicenter map (**a**) and South–North vertical projection (**b**) of the seismicity recorded during GRT-1 hydraulic stimulation (yellow circles), including the following crisis of July (green circles); injection flow rate, wellhead pressure and downhole overpressure over time (**c**) in parallel with the seismic rate per 15 min and the local magnitude (**d**); seismic rate per 15 min and local magnitude of the earthquakes recorded during the July crisis while no injection operation was on-going (**e**)

1800 m long and less than 500 m wide. The best least-squares fitting plane passing through the hypocenters is oriented N1° E, dipping 89° W, i.e., almost vertical. Most of the hypocenters were located between 1200 and 2000 m depth. The events at approximately 2000-m depth were located near the injection depth, whereas shallower events were located North of the injection. The earthquakes associated with the July 2013 burst extended the main stimulation cloud further NNE, in a N13° E direction, and a slight overlap between the hypocenters of both sequences was observed. This burst of seismicity was concentrated at two different depth intervals, between 1300 and 1500 m in the sedimentary layers, above the Muschelkalk, and between 1900 and 2100 m near the interface between the basement and sedimentary cover.

During the hydraulic stimulation, 80% of the hypocenters exhibited uncertainty between ±35 m and ±255 m, with a median of ±95 m, whereas during the burst, 80% of the hypocenters exhibited uncertainty between ±35 m and ±180 m, with a median of ±60 m.

Discussion

Occurrence of seismicity

Despite the injection temperature being similar in thermal and hydraulic stimulations (about 10 °C), the main difference lies in the injection flow rate. In a thermal stimulation, the flowrate is reduced to predominantly activate thermal effects contrarily to hydraulic stimulation that would enhance permeability to elevated pore pressure and shear slip of pre-existing fractures. According to Vidal et al. (2016), thermal stimulation is typically performed to enhance the near-well field permeability, which may have been reduced by drilling (cuttings and mud clogging feed zones), and thus this stimulation is generally performed immediately after drilling. As modeled by Gentier et al. (2004), during cold injection, thermal microcracking of quartz within the fractured zone is observed, which creates preferential flow paths and thus leads to preferential cooling in these fractures. At Rittershoffen, all identified permeable fractures are associated with quartz veins, which could enhance the thermal effect of cold reinjection through the fractured zones (Vidal et al. 2019). This technique is not usually applied to EGS geothermal wells in the URG, but has produced satisfactory results in high-temperature systems in volcanic environments.

During the GRT-1 thermal stimulation, seismicity started 26 h after the beginning of the injection, or 21 h after the WHP reached 2.8 MPa at 15 L/s (Fig. 8). Interestingly, this WHP was the largest observed over the entire operation and was also measured immediately after the 15 to 20 L/s and the 20 to 25 L/s injection steps. The lack of seismicity at the beginning of injection indicates that uncritically stressed zones connected to the open-hole existed and/or that rock cohesion was present. In the first case, it means that substantial pore pressure increase is needed to reach the Coulomb failure envelop, the latter meaning that the rock can sustain shear stress even though effective normal stress is null. From another perspective, the seismicity began 3 h following constant injection at 20 L/s and when the WHP was decreasing, which is evidence of increased injectivity and enhanced fluid circulation in the formation. This observation suggests that neither the flow rate nor the pressure observed when the first event occurred were at the origin of the seismicity, but rather delayed

(thermo-) mechanical effects on the rock mass due to the earlier part of the injection. Most of the seismicity occurred at the end of the 20-L/s injection plateau, when the WHP was increasing, and during the first half of the 25-L/s injection plateau. Then, the seismic rate decreased significantly while the injection was on-going at 25 L/s but the WHP was decreasing again. Finally, a last burst of seismicity was observed 11 h before injection ended. Thus, seismicity occurred only during a relatively short period of the injection.

Two months after thermal stimulation, the pre-stimulation test, chemical stimulation, hydraulic stimulation and injectivity test were conducted (Fig. 9). The seismic activity associated with these operations began only 6 h after start of the hydraulic stimulation, when the flow rate increased from 26.5 to 40 L/s, and the WHP reached 1.5 MPa (DHP = 1.8 MPa). Therefore, no seismicity was recorded during the pre-stimulation test, neither during the chemical stimulation nor during the injectivity test. The first two operations involved a limited volume of injected fluid, 626 m^3, which represents approximately 1/6 of the volume injected during thermal stimulation. Moreover, the injections were conducted at a maximum flow rate of 27 L/s and WHP of 2.5 MPa, which are levels not exceeding those observed during thermal stimulation, and under an injectivity index that was similar to that observed when the thermal stimulation ended (1.2 L/s/bar). Aware of the stimulation history, we would interpret the delayed seismicity to be a rock stress memory effect rather than a result of aseismic slips or creeping as suggested by Lengliné et al. (2017). Nonetheless, the latter cannot be excluded, especially for the first part of the thermal stimulation and if we consider that clay in fractured zones due to hydrothermal alteration could favor creeping rather than shearing (Meller and Kohl 2014). The rock stress memory effect implies that repeated loading of a rock mass generates seismicity only when and where maximum stress previously experienced is exceeded. Also known as the "Kaiser effect" (Kaiser 1950; Lavrov 2003), this characteristic has been observed in many EGS sites during forced fluid injection operations, e.g., Soultz-sous-Forêts (Dorbath et al. 2009), Cooper Basin—Australia (Baisch et al. 2015) and Berlín—El Salvador (Kwiatek et al. 2014). Nonetheless, in the present case, seismicity began only once the injection flow rate exceeded the largest rate applied (27 L/s) but at a WHP that was lower than previously measured (1.5 MPa vs. 2.8 MPa), which strictly differs from the Kaiser effect. This observation may be an evidence that the chemical stimulation was effective by creating new fluid pathways, not hydraulically stimulated yet.

Once seismicity began during the hydraulic stimulation, it continuously occurred and exhibited increasing seismic rates in correlation with increasing flow rates, except when the 60 to 70 L/s step was preceded by a 20-min injection at 27 L/s. A decrease in the seismicity rate was also observed during the 40-L/s injection plateau and when the WHP (and DHP) began to decrease, implying an increase of well injectivity, which was also observed at the end of the thermal stimulation. Thus, the decrease in seismicity is linked to an increase in injectivity throughout the course of the injection. Furthermore, seismicity almost vanished once the injection step-down phase began, which was also the case for the thermal stimulation, and no event was identified during the injectivity test following the hydraulic stimulation (except a single episode

approximately 1.5 h after injection stopped). These observations could also be interpreted as evidence of the Kaiser effect.

Figure 11 presents the distribution of the number of earthquakes above a minimum magnitude as a function of the injected volume for the thermal and hydraulic stimulations. The lowest minimum magnitude applied in both cases corresponds to the estimated magnitude of completeness (Fig. 12). For the hydraulic stimulation, the isolated burst of seismicity in July 2013 is not considered in the plot. As observed, there is no linear relation between both parameters during the thermal stimulation. During hydraulic stimulation, however, a linear tendency is observed after the first 500 m^3 are injected. This change in behavior may reflect an initialization phase of the main physical processes that induce seismicity and/or are a result of the previously conducted thermal stimulation. Deviation from the linear tendency was also observed and was expected; we noticed previously that seismicity decreased with increasing injectivity, and the seismicity rate increased with the injection steps, which implies hydro-mechanical coupling. Thus, the seismogenic index concept proposed by Shapiro et al. (2007) may not be applicable in a simple manner to the present case and that the underlying hypotheses are not fully satisfied. Specifically, it is questionable whether the pressure front diffusion in an infinite and homogeneous medium would be the mechanism responsible for controlling the seismicity occurrence (Cornet 2000).

Magnitude distribution

Figure 12 presents the frequency–magnitude distribution of the seismicity, which was identified during the GRT-1 thermal stimulation (145 events), the hydraulic stimulation (781 events), the following burst (152 events), and the drilling of GRT-2 (168 events). Given the low number of earthquakes recorded during the drilling of GRT-1, they are not considered in this analysis. As observed, a Gutenberg–Richter power law can explain more than 95% of the frequency–magnitude distribution of the seismic events at the given magnitudes of completeness (M_C). The M_C for these periods is very similar,

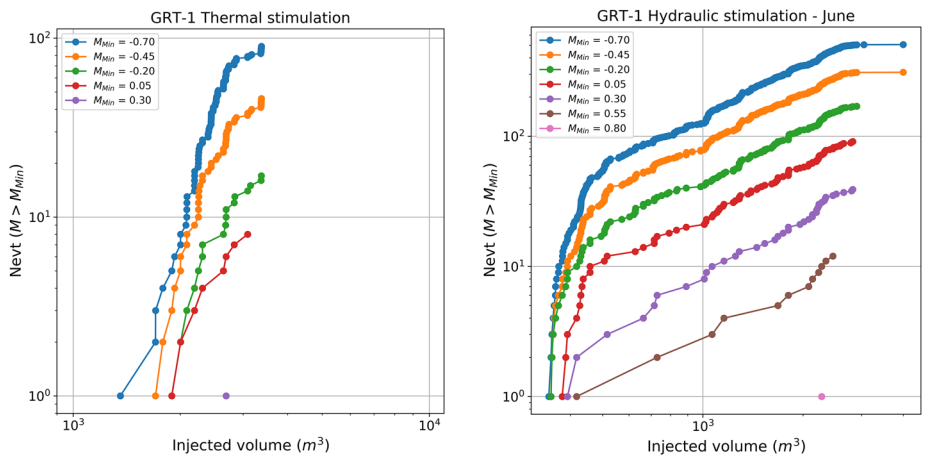

Fig. 11 Distribution of the number of earthquakes above a minimum magnitude (M_{Min}) as a function of the injected volume for the thermal stimulation (left) and hydraulic stimulation (right)

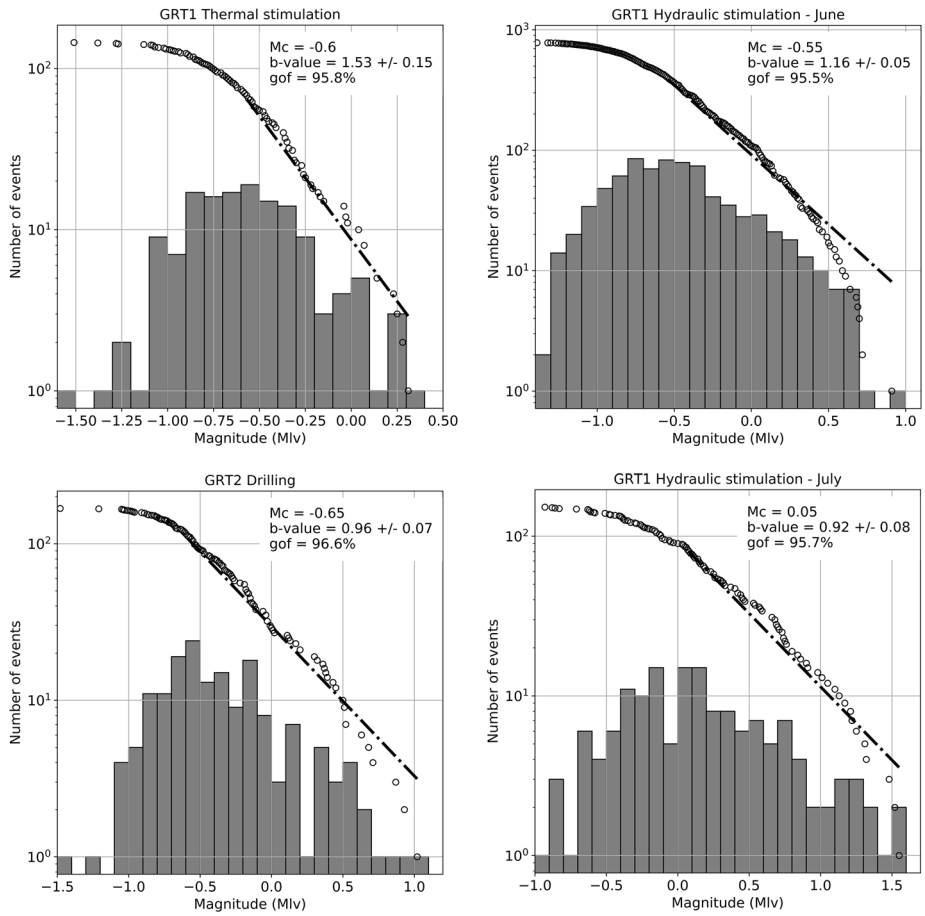

Fig. 12 Frequency–magnitude distribution of induced earthquakes: cumulative number (black circles) and histogram (gray bars), and an estimate of the magnitude of completeness and b-values. The results are given for the GRT-1 thermal stimulation (top left), GRT-2 drilling (bottom left), GRT-1 hydraulic stimulation—June (top right) and July burst (bottom right). The axis scales are different among the plots

approximately $M_C = -0.6$, except for the seismicity burst in July 2013, where $M_C = 0.05$. The occurrence of the seismicity during the seismicity burst, primarily between 7:00 and 9:00, which is when anthropogenic noise is relatively high, may explain the higher observed M_C value.

During the thermal stimulation and hydraulic stimulation, the *b*-values were estimated to 1.53 ± 0.15 and 1.16 ± 0.05, respectively. These are significantly higher than the typical tectonic value of 1, although only 42 events were used to calculate the *b*-value during the thermal stimulation (against 107 for the hydraulic stimulation). However, such high values are very common in injection-induced seismicity (Bachmann et al. 2011; Cuenot et al. 2008; Dorbath et al. 2009) and may be interpreted as the creation or reopening of small cracks and fractures in the rock mass due to high stress variation near the injection interval (El-Isa and Eaton 2014; Scholz 1968; Zang et al. 2014). Furthermore, the larger *b*-value measured during thermal stimulation may indicate relatively higher volumetric effects than the hydraulic stimulation, if not due to the low number of event used to calculate it. Thermal stimulation is supposed to activate thermomechanical effects and, to a lesser extent, hydro-mechanical effects, thus resulting in different rock responses.

In particular, the variable thermal properties of the minerals constituting the stimulated rock would lead to greater homogeneous breakdown of the matrix near the cold front. In the granite, fractures filled with secondary euhedral quartz (Glaas et al. 2018a, b) could be prone to thermal cracking (Wang et al. 1989). The event burst in July 2013 and the events induced by GRT-2 drilling, conversely, exhibit *b*-values of 0.92 ± 0.08 and 0.96 ± 0.07, respectively, which is more consistent with the reactivation of existing faults. In these periods, 61 and 75 events, respectively, could be used to calculate these values. These measurements corroborate the variation in the *b*-value between the hydraulic stimulation and the subsequent burst that was mentioned by Lengliné et al. (2017). They also highlight that different structures of different scales were activated by the hydraulic stimulation.

During the GRT-1 thermal and hydraulic stimulations, there was no tendency for higher magnitude events to occur as the stimulation was on-going.

Finally, the largest magnitude earthquakes observed during the thermal stimulation were much weaker than those of the hydraulic stimulation. Both stimulations involved the same amount of injected fluid; however, when considering the hydraulic stimulation as being complementary of the thermal stimulation (and chemical stimulation), this observation is in accordance with the general idea that the largest induced earthquake is related to the injected volume (Galis et al. 2017; McGarr 2014). However, this argument will not be further investigated because previously discussed observations suggest that the seismogenic response is more complex than the assumptions made in these modeling approaches.

Spatial distribution

In Fig. 13, the epicenter map shows that the cloud of seismicity associated with the thermal and hydraulic stimulations of GRT-1, as well as the July 2013 burst of seismicity, extends from the injection depth up to the GRT-2 well (which did not exist at that time) along an approximately N5° E vertical plane. The depth range of the cloud is relatively large. The deepest part roots in the granite and at the Buntsandstein–granite interface, which also corresponds to the intersection of the Rittershoffen fault with the well. Thus, the events clustered at approximately ~2000-m depth and extending to the north possibly occurred on the Rittershoffen fault, as also proposed by Lengliné et al. (2017). The shallowest part of the cloud reaches the 1300- to 1500-m depth interval, in the Keuper formation above the Muschelkalk. Thus, overall, the cloud appears to highlight a major vertical structure. Nonetheless, the observed vertical extension is questionable. First, this extension from more than 500 m cannot be a consequence of the location uncertainties, which are smaller than ± 255 m for more than 80% of the events. Second, the vertical distance to the injection point is relatively large, of the same order as the horizontal distance to the injection point. Such a development of seismicity is not in accordance with the expected normal- to strike–slip faulting regime of the region (Azzola et al. 2019; Cornet et al. 2007; Hehn et al. 2016), which favors a horizontal (rather than vertical) extension of seismicity. Third, the observed vertical distribution does not follow the dip of the Rittershoffen fault and would require the presence of another fault that was not identified, neither from drilling logs nor from active seismic processing. Fourth, the Keuper formation is not suspected to be very seismogenic because it is predominantly

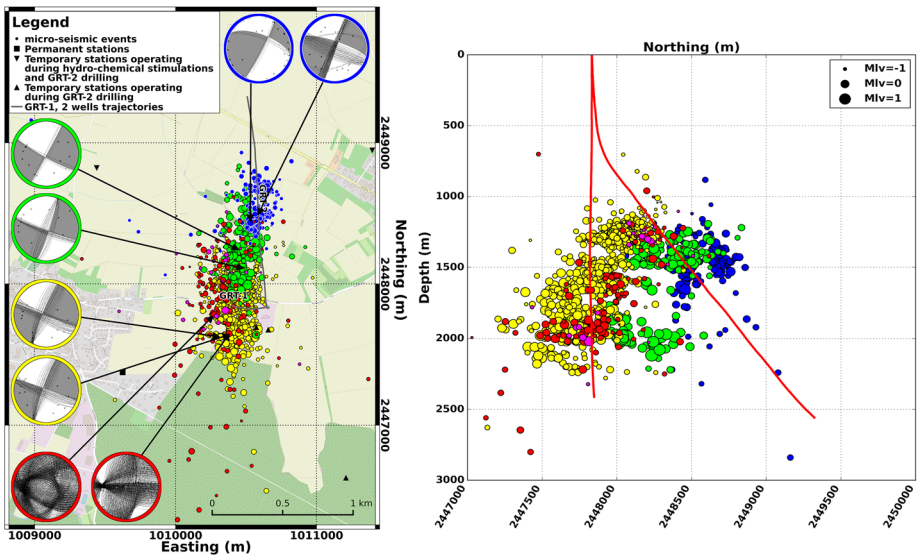

Fig. 13 Epicenter map (left) and South–North vertical projection (right) of the seismicity recorded during the development of the Rittershoffen deep geothermal site: GRT-1 drilling (magenta circles), thermal stimulation (red circles), hydraulic stimulation (yellow circles), burst of seismicity (green circles) and GRT-2 drilling (blue circles). Focal mechanisms have been computed for two representative events for each seismogenic period (except for GRT-1 drilling)

composed of evaporates and clays, which have a rather rheological ductile behavior. Moreover, it is noteworthy that, first, absolute locations are considered, even though being calibrated until the Muschelkalk. Second, the seismic network was composed of the permanent stations during the thermal stimulation with a few additional temporary stations: five stations during the hydraulic stimulation and eight stations during the July burst. All stations were exclusively located in the northern part of the GRT-1 well (Fig. 5). As discussed by Kinnaert et al. (2016), a large coverage gap may lead to strong uncertainties in the location and, interestingly, the average inclination of the seismic clouds (especially during hydraulic stimulation) is consistent with the location uncertainty direction. Further investigations highlighted a tendency of the hypocenters to belong to the deeper cluster when the number of seismic phases selected to locate an event was larger. Thus, the combined northern and vertical extension of the seismic events located south of the network may be, to some extent, a trade-off between depth and time resolution of the hypocenters due to the approximately exclusive northern coverage of the network prior to the GRT-2 drilling. (Such a trade-off could also explain both clusters associated with GRT-1 drilling.) Although relative earthquake location by double-differences (Poliannikov et al. 2013; Waldhauser and Ellsworth 2000) are beyond the scope of this paper, they may minimize or remove such effects by adding more constraints in the likelihood function of the earthquake hypocenters and origin times (Poliannikov et al. 2013). Consequently, the apparent vertical extension of the "GRT-1 cloud", especially up to 1300 m, and its apparent connection with the seismicity recorded during GRT-2 drilling should be further investigated before providing any definitive conclusions.

The suspected Kaiser effect highlighted by the occurrence of seismicity during stimulations should be supported by the location of the associated hypocenters. The Kaiser

effect is clearly observed between the seismicity occurring during the hydraulic stimulation and the following burst of seismicity (Fig. 13). Indeed, the July burst of seismicity is exclusively located at the northern rim of the seismicity induced during the hydraulic stimulation itself. However, the relatively widespread cloud of events associated with the thermal stimulation appears to cover a volume similar to the seismogenic zone of the hydraulic stimulation. Indeed, no evolution of the hypocenter distance to the well as a function of time was observed in this study. Yet, without relative location of the seismicity, detailed spatio-temporal interpretation is limited because the absolute hypocenter uncertainties can range between ±20 m and ±250 m. Figure 14 shows the hypocenter uncertainty as a function of the earthquake magnitude, for each period. As seen, the seismicity induced during thermal stimulation is less certain (median of ±135 m) than seismicity induced during hydraulic stimulation (median of ±95 m). This is first due to the smaller seismic network monitoring the thermal stimulation and second to lower magnitude events induced during that period (see Fig. 12). One can also note that the smallest hypocenter uncertainties are associated with earthquakes recorded during GRT-2 drilling (blue circles), that is when the monitoring network was the most complete. As expected, Fig. 14 highlights that the less certain hypocenters are associated with small magnitude events. However, small magnitude events do not necessarily lead to large hypocenter uncertainties because the seismic background noise also affects the imprecision of the P- and S-phase picking.

Focal mechanisms

Focal mechanisms were determined for earthquakes, which occurred during the thermal and hydraulic stimulations, the July burst and the GRT-2 drilling. They were assumed double-couples and were determined using FOCMEC (Snoke 2017) with

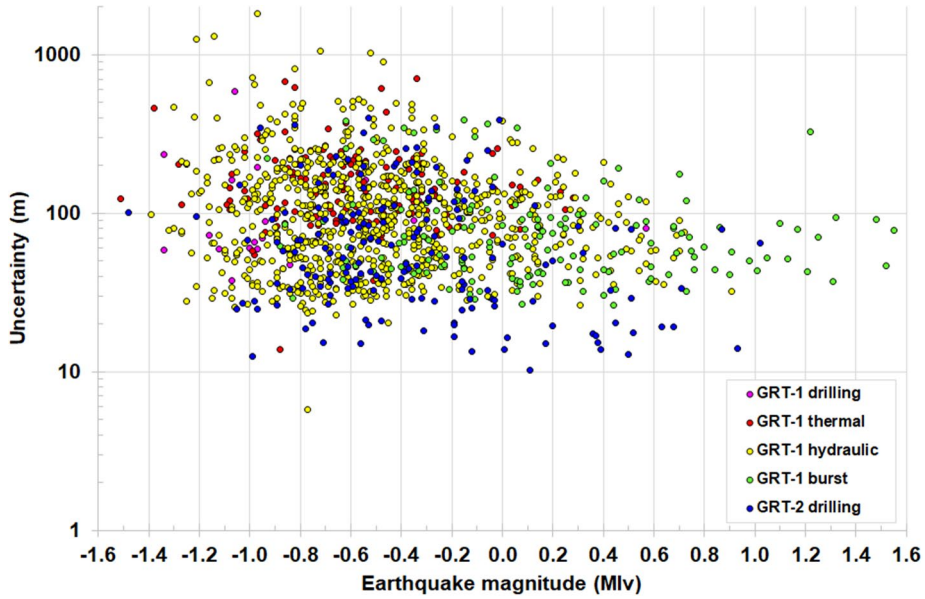

Fig. 14 Hypocenter uncertainty as a function of the earthquake magnitude for the GRT-1 drilling (magenta circles), thermal stimulation (red circles), hydraulic stimulation (yellow circles), burst of seismicity (green circles) and GRT-2 drilling (blue circles). Please note the logarithmic scale of the vertical axis

the polarity of the P-wave arrivals. Relative weighting of the polarities was applied to allow possible polarity mismatch close to the focal planes. Two earthquakes per seismogenic period were considered. To maximize the chances of determining the focal mechanism on the relatively noisy data, the earthquakes with the highest number of P-wave picks and the highest magnitudes were preselected. Then, the earliest and latest events of the sequence were chosen to form the pair assuming the chance that the focal mechanisms would differ higher. Table 3 gives the characteristics of the eight inverted mechanisms and the corresponding earthquake. Among all focal plane solutions, the solution associated with the median plane dip is given on the lower hemisphere in gray in Fig. 13, as well as all other possible solutions (with a maximum of 500 solutions).

As seen, all earthquakes induced during and after hydraulic stimulation and during drilling of GRT-2 have sinistral strike–slip focal mechanisms. The network coverage for the earthquakes induced during thermal stimulation is clearly too small and prevents determining the rupture geometry unambiguously. However, sinistral strike–slip is one of the numerous possible solutions.

These results show that a common rupture with strike, dip and rake in the intervals 195 to 210° N, 85 to 90° and − 5 to 20°, respectively, could be attributed to the earthquakes associated with the stimulation operations, at least for the strongest ones. Interestingly, Azzola et al. (2019) identified a maximal horizontal stress direction of N15° in the Buntsandstein, which is consistent with the observed strike range and the earthquake depths. The corresponding focal plane is relatively consistent with the earthquake distribution as well as the Rittershoffen fault orientation. Hence, during thermal and hydraulic stimulations, the Rittershoffen fault was undoubtedly activated

Table 3 Characteristics of the earthquakes for which focal mechanism was determined

Period	Origin time	Easting (m)	Northing (m)	Depth (m TVD MSL)	Mlv	N_{POL}	Dip (°)	Strike (°)	Rake (°)
Thermal stimulation	2013-04-25 01:59:33	2,447,782	1,010,272	1960	0.31	5	–	–	–
Thermal stimulation	2013-04-25 03:38:00	2,447,649	1,010,380	1901	0.23	6	–	–	–
Hydraulic stimulation	2013-06-27 23:25:59	2,447,636	1,010,372	1993	0.69	14	80	199	− 3
Hydraulic stimulation	2013-06-28 01:45:44	2,447,624	1,010,312	1860	0.54	12	80	202	3
July burst	2013-07-02 04:53:52	2,448,243	1,010,448	2023	1.21	14	87	29	− 10
July burst	2013-07-02 05:11:18	2,448,113	1,010,473	1480	1.31	12	81	188	− 5
GRT-2 drilling	2014-05-26 13:33:25	2,448,495	1,010,587	1517	0.01	18	87	200	− 9
GRT-2 drilling	2014-05-26 14:18:29	2,448,456	1,010,532	1656	1.02	31	80	28	39

The column N_{POL} gives the number of P-wave polarities used to determine the focal mechanism. The focal plane angles follow the standard convention (Aki and Richards 1980)

beside other smaller faults or fractures as suggested by the *b*-values higher than 1. The seismicity recorded in July would belong exclusively to that structure, which is supported by the *b*-value of 0.92. These results also indicate that the hypothesis of attributing the local magnitude calculated at the KUHL station to the earthquakes is reasonable. Moreover, P-wave polarity at station KUHL is always negative (dilation) and supports this hypothesis in case of undetermined focal mechanism.

Conclusion

We presented and discussed the seismicity associated with the Rittershoffen field development, its occurrence, its magnitude distribution and its spatial distribution in the light of all field operations and their injection parameters. The development of the Rittershoffen geothermal reservoir was associated with unfelt seismicity. More than 1300 earthquakes were processed. Mud losses in the Muschelkalk formation, in the course of the drilling of both wells of the doublet, led to several tens (GRT-1) to several hundreds (GRT-2) of events located near the wells, all with local magnitudes smaller than 1.0.

Most of the recorded seismicity, 85%, was induced directly or indirectly by the GRT-1 stimulations. The initial 2.5-day thermal stimulation was the first operation that induced substantial seismicity. The latter, however, was recorded more than 1 day after the beginning of the injection and did not coincide with an abrupt change of the injection flow rate, nor the maximum injection flow rate (25 L/s), nor a WHP peak, nor the maximum WHP (2.8 MPa), showing that uncritically stressed zones connected to the open-hole may exist or/and that rock cohesion should be considered. Furthermore, a reduction of the seismic rate related to an increase of injectivity was observed during thermal and hydraulic stimulations. There was no clear evidence of a linear relationship between the number of recorded earthquakes and the injected volume.

Several observations are interpreted as a typical signature of the rock stress memory effect, or "Kaiser" effect, e.g., the lack of seismicity recorded during the pre-stimulation test of GRT-1 (the first injection following the thermal stimulation), during the chemical stimulations, for the first 6 h of the hydraulic stimulation and during the final injection test. This Kaiser effect signature was difficult to further support based on the earthquake hypocenters obtained from absolute location methods that are not sufficiently accurate, with the exception of the earthquakes associated with the burst of seismicity, which were located to the north of the previously active zone.

During stimulations, *b*-values were larger than 1.1, which may be interpreted as the creation or reopening of small cracks and fractures in the rock mass due to high stress variation near the injection. However, *b*-values decreased to 0.9 during the burst of seismicity following the hydraulic stimulation, which is interpreted as the reactivation of an existing major structure—possibly the Rittershoffen fault. During the seismicity burst, the largest event induced at Rittershoffen, Mlv = 1.6, occurred and the events typically had larger magnitudes than previously observed.

The absolute location of the seismicity as well as the determination of a few focal mechanisms support the idea that pre-existing faults were reactivated above the intersection between the Rittershoffen fault and the GRT-1 well, in the Buntsandstein–basement interface during the thermal and the hydraulic stimulations. The limited coverage of the seismic network before GRT-2 drilling, however, prevents strong conclusions

from being made on the veracity of the depth extension of the stimulated zone up to the Keuper formation, thus necessitating further investigations. The relative locations of future earthquakes will minimize systematic bias and will improve the geometrical interpretation of induced seismicity to understand better the development and the behavior of the Rittershoffen geothermal reservoir.

Supplementary information

Supplementary information accompanies this paper at https://doi.org/10.1186/s40517-020-0155-2.

Additional file 1. Reference catalogue of the 1348 earthquakes discussed in the paper. For each event, it contains the following parameters, in the following order: origin date and time (UTC time), northing and easting of epicenter location (Lambert II extended coordinate system, meters), depth (true vertical depth below sea level, meters), local magnitude (vertical component), azimuth and dip of the small uncertainty axis (Az1, Dip1, degrees), azimuth and dip of the middle uncertainty axis (Az2, Dip2, degrees), smallest-, middle- and largest-uncertainties (Len1, Len2 and Len3, meters) and the recorded period: 0–GRT-1 drilling, 1–GRT-1 thermal stimulation, 20–GRT-1 hydraulic stimulation, 21–GRT-1 burst of seismicity and 3–GRT-2 drilling. See text for more details on how these values were calculated.

Abbreviations

ANR: French National Research Agency (Agence Nationale pour la Recherche); DCF: Deutschland longwave signal transmitted by station Mainflingen near Frankfurt am Main; DHP: downhole pressure; ECOGI: Operating company of the Rittershofen geothermal field (Exploitation de la Chaleur d'Origine Géothermale pour l'Industrie); EGS: enhanced geothermal system; EOST: École et Observatoire des Sciences de la Terre (Earth Science School and Observatory); ESG: ES-Géothermie; GFZ: German Research Centre for Geosciences; GIPP: Geophysical Instrument Pool Potsdam; GL: ground level; M_C: magnitude of completeness; MD: measured depth at ground Level; Mlv: vertical local magnitude; MSL: mean sea level; MWth: thermal megawatt; My: million years; STA/LTA: short time average over long time average; TVD: true vertical depth; URG: Upper Rhine Graben; UTC: coordinated universal time; Vp: P-wave velocity; Vs: S-wave velocity; VSP: vertical seismic profile; WHP: wellhead pressure.

Acknowledgements

The authors thank the ECOGI for sharing data with the scientific community. We thank the Geophysical Instrument Pool Potsdam of the GFZ German Research Centre for Geosciences for providing the temporary seismological units deployed by KIT. The deployment of the temporary network received support from the excellence laboratory "LabEx G-EAU-THERMIE PROFONDE" (University of Strasbourg) as part of the French "Investments for the future" of the French National Research Agency. We also thank H. Wodling, H. Jund and C. Schnell from EOST for their support in the deployment of the temporary seismic network; C. Baujard and A. Genter from ESG, who shared their experience and knowledge concerning field operations; J. Schmittbuhl and O. Lengliné from EOST for their fruitful discussions; and Nicolas Perrinel from ESG for his work on the 3D velocity model. We also would like to thank Gempa GmbH and the GFZ for providing and maintaining the SeisComp3 software. The authors are grateful to ADEME, the French Agency for Energy and Environment for co-funding this study in the framework of the EGS Alsace collaborative research project.

Authors' contributions

All authors worked to generate the reference seismological catalogue presented in this paper. VM and EG analyzed the data and wrote the initial manuscript. MG completed the seismic monitoring and processing sections. All authors contributed to the final manuscript. All authors read and approved the final manuscript.

Funding

ECOGI funded a portion of the monitoring network. The deployment of the temporary seismic network received funds from the excellence laboratory "LabEx G-EAU-THERMIE PROFONDE" (University of Strasbourg), as part of the French "Investments for the future" of the French National Research Agency. This work was also conducted in the frame of the DESTRESS project, which received funding from the European Union's Horizon 2020 research and innovation program under grant agreement no. 691728. The French national research agency (ANR) also supported this work under grant agreement ANR-15-CE06-0014-04, referred to as Cantare Alsace.

Availability of data and materials

The referenced seismic catalogue analyzed during this study is included in this published article as an Additional file 1. The raw seismic files acquired using the temporary seismic monitoring network are available upon request from the Geophysical Instrument Pool Potsdam of the GFZ German Research Centre for Geosciences by referencing the Scientific Technical Report of Gaucher et al. (2018).

Competing interests

The authors declare that they have no competing interests.

Author details

[1] ES-Geothermie, 5 rue de Lisbonne, Le Belem, 67300 Schilitigheim, France. [2] Division of Geothermal Research, Institute of Applied Geosciences, Karlsruhe Institute of Technology, Kaiserstraße 12, 76131 Karlsruhe, Germany. [3] Université de Strasbourg, CNRS, EOST UMS 830, 67000 Strasbourg, France.

Appendix

See Table 4.

Table 4 Seismic station locations (in the extended Lambert II Cartesian coordinate system) and associated recording periods: *P*1: from beginning of monitoring; *P*2: from GRT-1 chemical and hydraulic stimulation; and *P*3: before GRT-2 drilling

Network	Station	Easting (m)	Northing (m)	Depth (m MSL)	*P*1	*P*2	*P*3
Permanent	BETS	1,009,624.3	2,447,374.9	− 146	1	1	1
	FORA	1,004,921.7	2,452,089.6	− 156	1	1	1
	GUNS	999,344.6	2,449,908.1	− 224	1	1	1
	KEFF	1,005,387.2	2,455,522.6	− 208	1	1	1
	KUHL	1,009,871.8	2,449,753	− 176	1	1	1
	LAMP	1,000,768.6	2,454,636.3	− 257	1	1	1
	OBER	1,012,458.4	2,451,824.5	− 177	1	1	1
	OPS	1,006,369.1	2,450,232.9	− 198	1	1	1
	RITT	1,012,306.7	2,447,654.7	− 138	1	1	1
	SCHW	1,005,375.8	2,447,345.1	− 143	1	1	1
	STUN	1,014,315.6	2,450,563.5	− 146	1	1	1
	SURB	1,003,874.7	2,449,430.3	− 203	1	1	1
Temporary	E3022	1,005,972.5	2,448,936.6	− 182	0	0	1
	E3024	1,007,780.7	2,443,765.9	− 156	0	0	1
	E3025	1,009,739.1	2,442,950.1	− 140	0	0	1
	E3030	1,013,616	2,444,769	− 136	0	0	1
	E3033	1,014,891.8	2,447,162.2	− 134	0	0	1
	E3034	1,011,363.2	2,452,718.8	− 150	0	0	1
	E3078	1,012,931.8	2,448,467	− 161	0	0	1
	E3087	1,006,194.1	2,445,682.7	− 160	0	0	1
	E3088	1,009,872.2	2,449,747.5	− 185	0	0	1
	E3091	1,014,489.8	2,449,656.8	− 129	0	0	1
	E3094	1,007,480.1	2,451,506.2	− 152	0	0	1
	E3096	1,010,572.3	2,447,695.7	− 153	0	0	1
	E3099	1,011,863.9	2,442,894.2	− 137	0	0	1
	E3100	1,010,661.2	2,447,676.4	− 153	0	0	1
	E3101	1,009,269.3	2,452,535.8	− 148	0	0	1
	E3300	1,013,394.7	2,449,956.1	− 129	0	0	1
	E3301	1,011,395.5	2,448,938.1	− 172	0	1	1
	E3302	1,009,983.8	2,451,388.6	− 145	0	0	1
	E3304	1,013,385.8	2,446,283	− 131	0	0	1
	E3305	1,011,216.5	2,446,617.3	− 149	0	0	1
	E3306	1,007,340.8	2,446,496.7	− 154	0	0	1
	E3307	1,009,955.2	2,444,680	− 139	0	0	1
	E3308	1,007,578.8	2,448,349.6	− 174	0	1	1
	E3310	1,008,593.7	2,445,272.5	− 147	0	0	1
	E3311	1,009,752.3	2,446,444.8	− 159	0	0	1
	E3312	1,015,300	2,445,164.7	− 128	0	0	1
	E3313	1,008,256.6	2,450,042	− 182	0	1	1
	E3314	1,014,234.2	2,448,519.4	− 147	0	0	1
	E3315	1,009,443.4	2,448,820	− 175	0	1	1
	E3316	1,012,177	2,444,781.8	− 132	0	0	1
	E3317	1,011,370.6	2,450,674.4	− 144	0	1	1

Received: 15 July 2019 Accepted: 10 January 2020
Published online: 05 February 2020

References

Aichholzer C, Duringer P, Orciani S, Genter A. New stratigraphic interpretation of the Soultz-sous-Forêts 30-year-old geothermal wells calibrated on the recent one from Rittershoffen (Upper Rhine Graben, France). Geotherm Energy. 2016;4(1):132.
Aki K. 17. Maximum Likelihood Estimate of b in the Formula logN = a-bM and its Confidence Limits. Bull Earthq Res Inst Univ Tokyo. 1965;43(2):237–9.
Aki K, Richards PG. Quantitative seismology, theory and methods. 1st ed. San Fransisco: W. H. Freeman and Co.; 1980. p. 557.
Azzola J, Valley B, Schmittbuhl J, Genter A. Stress characterization and temporal evolution of borehole failure at the Rittershoffen geothermal project. Solid Earth. 2019;10:1155–80. https://doi.org/10.5194/se-10-1155-2019
Bachmann CE, Wiemer S, Woessner J, Hainzl S. Statistical analysis of the induced Basel 2006 earthquake sequence: introducing a probability-based monitoring approach for enhanced geothermal systems. Geophys J Int. 2011;186(2):793–807.
Baillieux P, Schill E, Edel J-B, Mauri G. Localization of temperature anomalies in the Upper Rhine Graben: insights from geophysics and neotectonic activity. Int Geol Rev. 2013;55(14):1744–62.
Baisch S, Rothert E, Stang H, Vörös R, Koch C, McMahon A. Continued geothermal reservoir stimulation experiments in the cooper basin (Australia). Bull Seismol Soc Am. 2015;105(1):198–209.
Bakun WH, Joyner WB. The ML scale in central California. Bull Seismol Soc Am. 1984;74(5):1827–43.
Baujard C, Genter A, Dalmais E, Maurer V, Hehn R, Rosillette R, Vidal J, Schmittbuhl J. Hydrothermal characterization of wells GRT-1 and GRT-2 in Rittershoffen, France: implications on the understanding of natural flow systems in the rhine graben. Geothermics. 2017;65:255–68.
Baujard C, Genter A, Cuenot N, Mouchot J, Maurer V, Hehn R, Ravier G, Seibel O, Vidal J. Experience from a successful soft stimulation and operational feedback after 2 years of geothermal power and heat production in Rittershoffen and Soultz-sous-Forêts plants (Alsace, France). Reno: Geothermal Resources Council Transactions; 2018. p. 2241–52.
Clinton J, Grigoli F, Diehl T, Kraft T, Scarabello L, Hermann M, Kaestli P, Boese M, Wiemer S. Advanced real-time monitoring for natural and induced seismic sequences. In: Geophyscial Research Abracts, vol. 20, EGU General Assembly; 2018. **(abstract: EGU2018-9480-2)**.
Cornet FH. Comment on 'Large-scale in situ permeability tensor of rocks from induced microseismicity' by S. A. Shapiro, P. Audigane and J.-J. Royer. Geophys J Int. 2000; 140(2): 465–9.
Cornet FH, Bérard T, Bourouis S. How close to failure is a granite rock mass at a 5 km depth? Int J Rock Mech Min Sci Geomech Abstracts. 2007;44(1):47–66.
Cuenot N, Genter A. Microseismic activity induced during recent circulation tests at the Soultz-sous-Forêts EGS power plant. In: World geothermal congress 2015. World Geothermal Congress, Melbourne, Australia. April 20–24. IGA; 2015.
Cuenot N, Dorbath C, Dorbath L. Analysis of the microseismicity induced by fluid injections at the EGS site of Soultz-sous-Forêts (Alsace, France): implications for the characterization of the geothermal reservoir properties. Pure Appl Geophys. 2008;165(5):797–828.
Deichmann N, Giardini D. Earthquakes induced by the stimulation of an enhanced geothermal system below Basel (Switzerland). Seismol Res Lett. 2009;80(5):784–98.
Dezayes C, Genter A, Valley B. Structure of the low permeable naturally fractured geothermal reservoir at Soultz. CR Geosci. 2010;342(7–8):517–30.
Dorbath L, Cuenot N, Genter A, Frogneux M. Seismic response of the fractured and faulted granite of Soultz-sous-Forêts (France) to 5 km deep massive water injections. Geophys J Int. 2009;177(2):653–75.
Duringer P, Aichholzer C, Orciani S, Genter A. The complete lithostratigraphic section of the geothermal wells at Rittershoffen (Upper Rhine Graben, eastern France): a key for future geothermal wells. BSGF Earth Sci Bull; in press.
Edel JB, Maurer V, Dalmais E, Genter A, Richard A, Letourneau O, Hehn R. Structure and nature of the Palaeozoic basement based on magnetic, gravimetric and seismic investigations in the central Upper Rhinegraben. Geotherm Energy. 2018;6(1):747.
El-Isa ZH, Eaton DW. Spatiotemporal variations in the b-value of earthquake magnitude–frequency distributions: classification and causes. Tectonophysics. 2014;615–616:1–11.
Équipe du projet GeORG. Potentiel géologique profond du Fossé rhénan supérieur. Parties 1 à 4; 2013. http://www.geopotenziale.eu. Accessed 5 Apr 2019.
Ester M, Kriegel H-P, Sander J, Xu X. A density-based algorithm for discovering clusters in large spatial databases with noise. In: International conference on knowledge discovery and data mining (AAAI), Portland, OR, USA. August 2–4; 1996.
Evans KF, Zappone A, Kraft T, Deichmann N, Moia F. A survey of the induced seismic responses to fluid injection in geothermal and CO2 reservoirs in Europe. Geothermics. 2012;41:30–54.
Galis M, Ampuero JP, Mai PM, Cappa F. Induced seismicity provides insight into why earthquake ruptures stop. Sci Adv. 2017;3(12):eaap7528.
Ganz B, Schellschmidt R, Schulz R, Sanner B. Geothermal energy use in Germany. In: European geothermal congress 2013. European Geothermal Congress, Pisa, Italy. June 3–7; 2013.
Gaucher E, Maurer V, Wodling H, Grunberg M. Towards a dense passive seismic network over Rittershoffen geothermal field. In: European geothermal workshop 2013b, Strasbourg, France. October 24–25; 2013.

Gaucher E, Schoenball M, Heidbach O, Zang A, Fokker PA, van Wees J-D, Kohl T. Induced seismicity in geothermal reservoirs: a review of forecasting approaches. Renew Sustain Energy Rev. 2015;52:1473–90.
Gaucher E, Maurer V, Grunberg M. Temporary passive seismic data acquired at Rittershoffen geothermal field (Alsace, France, 2013–2014). Scientific Technical Report, GIPP Experiment and Data Archive, Potsdam, Germany; 2018.
Genter A, Evans K, Cuenot N, Fritsch D, Sanjuan B. Contribution of the exploration of deep crystalline fractured reservoir of Soultz to the knowledge of enhanced geothermal systems (EGS). Comptes Rendus Geosci. 2010;342(7–8):502–16.
Genter A, Baujard C, Cuenot N, Hehn R, Maurer V, Mouchot J, Seibel O, Vidal J. Exploiting fractured granites for producing heat or electricity—dream or reality? In: 80th EAGE conference and exhibition 2018. 80th EAGE conference and exhibition 2018, Copenhagen, Denmark. 6/11/2018–6/14/2018. EAGE Publications BV Netherlands; 2018.
Gentier S, Hosni A, Dezayes C, Genter A. Modélisation du comportement hydro-thermomécanique des milieux fracturés (module 1), Projet GEFRAC, Open file report No. BRGM/RP-52702-FR; 2004.
Glaas C, Genter A, Girard JF, Patrier P, Vidal J. Correction to: how do the geological and geophysical signatures of permeable fractures in granitic basement evolve after long periods of natural circulation? Insights from the Rittershoffen geothermal wells (France). Geotherm Energy. 2018a;6(1):243.
Glaas C, Genter A, Girard JF, Patrier P, Vidal J. How do the geological and geophysical signatures of permeable fractures in granitic basement evolve after long periods of natural circulation? Insights from the Rittershoffen geothermal wells (France). Geotherm Energy. 2018b;6(1):54.
Grigoli F, Boese M, Scarabello L, Diehl T, Weber B, Wiemer S, Clinton JF. Picking vs Waveform based detection and location methods for induced seismicity monitoring. In: Geophyscial Research Abracts, vol. 19, EGU General Assembly; 2017. **(abstract: EGU2017-10562)**.
Hanka W, Saul J, Weber B, Becker J, Harjadi P, Fauzi, GITEWS Seismology Group. Real-time earthquake monitoring for tsunami warning in the Indian Ocean and beyond. Nat Hazards Earth Syst Sci. 2010;10(12):2611–22. https://doi.org/10.5194/nhess-10-2611-2010
Hehn R, Genter A, Vidal J, Baujard C. Stress field rotation in the EGS well GRT-1 (Rittershoffen, France). In: European geothermal congress, Strasbourg, France. September 19–26; 2016.
Kaiser J. An investigation in the occurence of noises in tensile tests or a study of acoustic phenomena in tensile tests. Ph.D. Thesis. Tech. Hoch. München, Germany; 1950.
Kendall JM, Butcher A, Stork AL, Verdon JP, Luckett R, Baptie BJ. How big is a small earthquake? Challenges in determining microseismic magnitudes. First Break. 2019;37(2):51–6.
Kinnaert X, Gaucher E, Achauer U, Kohl T. Modelling earthquake location errors at a reservoir scale: a case study in the Upper Rhine Graben. Geophys J Int. 2016;206:861–79.
Küperkoch L, Olbert K, Meier T. Long-term monitoring of induced seismicity at the Insheim geothermal site, Germany. Bull Seismol Soc Am. 2018;108(6):3668–83.
Kwiatek G, Bulut F, Bohnhoff M, Dresen G. High-resolution analysis of seismicity induced at Berlín geothermal field, El Salvador. Geothermics. 2014;52:98–111.
Lavrov A. The Kaiser effect in rocks: principles and stress estimation techniques. Int J Rock Mech Min Sci. 2003;40(2):151–71.
Lengliné O, Boubacar M, Schmittbuhl J. Seismicity related to the hydraulic stimulation of GRT1, Rittershoffen, France. Geophys J Int. 2017;208(3):1704–15.
Lomax A. The NonLinLoc home page; 2018. http://alomax.free.fr/nlloc/. Accessed 15 May 2018.
Lomax A, Curtis A. Fast, probabilistic earthquake location in 3D models using oct-tree importance sampling. Geophys Res Abstr 3:955; 2001. http://www.alomax.net/nlloc/octtree. Accessed 15 May 2018.
Lomax A, Virieux J, Volant P, Berge-Thierry C. Probabilistic earthquake location in 3D and layered models. In: Thurber C, Rabinowitz N, editors. Advances in seismic event location, vol. 18., Modern approaches in geophysics-Dordrecht: Springer; 2000. p. 101–34.
Lomax A, Michelini A, Curtis A. Earthquake location, direct, global-search methods. In: Meyers RA, editor. Encyclopedia of complexity and systems science. New York: Springer; 2009. p. 2449–73.
Majer EL, Baria R, Stark M, Oates S, Bommer J, Smith B, Asanuma H. Induced seismicity associated with enhanced geothermal systems. Geothermics. 2007;36(3):185–222.
Maurer V, Cuenot N, Gaucher E, Grunberg M, Vergne J, Wodling H, Lehujeur M, Schmittbuhl J. Seismic monitoring of the Rittershoffen EGS project (Alsace, France). In: World geothermal congress 2015. World geothermal congress, Melbourne, Australia. April 20–24. IGA; 2015.
Maurer V, Perrinel N, Dalmais E, Richard A, Plevy L, Genter A. Towards a 3D velocity model deduced from 2D seismic processing and interpretation of in Northern Alsace (France). In: European geothermal congress 2016, Strasbourg, France. September 19–26; 2016.
McGarr A. Maximum magnitude earthquakes induced by fluid injection. J Geophys Res Solid Earth. 2014;119(2):1008–19.
Megies T, Wassermann J. Microseismicity observed at a non-pressure-stimulated geothermal power plant. Geothermics. 2014;52:36–49.
Meller C, Kohl T. The significance of hydrothermal alteration zones for the mechanical behavior of a geothermal reservoir. Geotherm Energy. 2014;2(1):12.
Nami P, Schellschmidt R, Schindler M, Tischner T. Chemical stimulation operations for reservoir development of the deep crystalline HDR/EGS system at Soultz-sous-Forêts (France). In: 33th workshop on geothermal reservoir engineering. 33th workshop on geothermal reservoir engineering, Stanford, CA, USA. January 28–30; 2008.
Poliannikov OV, Prange M, Malcolm A, Djikpesse H. A unified Bayesian framework for relative microseismic location. Geophys J Int. 2013;194(1):557–71.
Portier S, Vuataz F-D, Nami P, Sanjuan B, Gérard A. Chemical stimulation techniques for geothermal wells: experiments on the three-well EGS system at Soultz-sous-Forêts, France. Geothermics. 2009;38(4):349–59.

Sanjuan B, Millot R, Innocent C, Dezayes C, Scheiber J, Brach M. Major geochemical characteristics of geothermal brines from the Upper Rhine Graben granitic basement with constraints on temperature and circulation. Chem Geol. 2016;428:27–47.
Schindler M, Baumgärtner J, Gandy T, Hauffe P, Hettkamp T, Menzel H, Penzkofer P, Teza D, Tischner T, Wahl G. Successful hydraulic stimulation techniques for electric power production in the Upper Rhine graben, Central Europe, In: World geothermal congress 2010. World geothermal congress, Bali, Indonesia. April 25–29; 2010.
Scholz CH. The frequency-magnitude relation of microfracturing in rock and its relation to earthquakes. Bull Seismol Soc Am. 1968;58(1):399–415.
Schumacher ME. Upper Rhine Graben: role of preexisting structures during rift evolution. Tectonics. 2002;21(1):6.
Shapiro SA, Dinske C, Kummerow J. Probability of a given-magnitude earthquake induced by a fluid injection. Geophys Res Lett. 2007;34(22):L22314.
Snoke AJ. FOCMEC: FOCal MEChanism determinations; 2017. p. 31. http://www.iris.edu/pub/programs/focmec/. Accessed 17 Sept 2018.
Tarantola A, Valette B. Inverse problems = quest for information. J Geophys. 1982;50:159–70.
Vidal J, Genter A, Schmittbuhl J. Pre- and post-stimulation characterization of geothermal well GRT-1, Rittershoffen, France: insights from acoustic image logs of hard fractured rock. Geophys J Int. 2016;206:845–60.
Vidal J, Hehn R, Glaas C, Genter A. How can temperature logs help identify permeable fractures and define a conceptual model of fluid circulation? an example from deep geothermal wells in the upper rhine graben. Geofluids. 2019;2019:1–14.
Waldhauser F, Ellsworth WL. A double-difference earthquake location algorithm: method and application to the Northern Hayward fault, California. Bull Seismol Soc Am. 2000;90(6):1353–68.
Wang HF, Bonner BP, Carlson SR, Kowallis BJ, Heard HC. Thermal stress cracking in granite. J Geophys Res Solid Earth Planets. 1989;94(B2):1745.
Wiemer S, Wyss M. Minimum magnitude of completeness in earthquake catalogs: examples from Alaska, the western United States, and Japan. Bull Seismol Soc Am. 2000;90(4):859–69.
Zang A, Oye V, Jousset P, Deichmann N, Gritto R, McGarr A, Majer E, Bruhn D. Analysis of induced seismicity in geothermal reservoirs—an overview. Geothermics. 2014;52:6–21.
Ziegler PA. European cenozoic rift system. Tectonophysics. 1992;208(1–3):91–111.

Publisher's Note